A molecular basis of somatotopic map formation

Authors: Kevin T. Sangster[1,2], Xinying Zhang[1,2], Daniel del Toro[3], Christina Sarantopoulos[1,2], Ashley M. Moses[4], Shreya Mahasenan[1], Daniel T. Pederick[4], Sophie Perreault[5], Catherine Fallet-Bianco[6,7], R. Brian Roome[8], Elena Seiradake[9,10], Liqun Luo[4], Artur Kania[1,2,11,12] *

Affiliations:

[1]Institut de Recherches Cliniques de Montréal (IRCM); Montréal, QC, Canada.

[2]Integrated Program in Neuroscience, McGill University; Montréal, QC, Canada.

[3]Department of Biomedical Sciences, Faculty of Medicine and Health Sciences, Institute of Neurosciences, IDIBAPS, CIBERNED, University of Barcelona; Barcelona, Spain.

[4]Department of Biology, Howard Hughes Medical Institute, Stanford University; Stanford, CA, USA.

[5]Azrieli Research Center at CHU Sainte-Justine; Montréal, QC, Canada.

[6]Department of Pathology, CHU Sainte-Justine; Montréal, QC, Canada.

[7]Department of Pathology and Cell Biology, Université de Montréal; Montréal, QC, Canada.

[8]Spinal Circuits and Plasticity Unit, National Institute of Neurological Disorders and Stroke; Bethesda, MD, USA.

[9]Department of Biochemistry, Oxford University; Oxford, UK.

[10]Kavli Institute for Nanoscience Discovery, University of Oxford; Oxford, UK.

[11]Division of Experimental Medicine, McGill University; Montréal, QC, Canada.

[12]Department of Anatomy and Cell Biology, McGill University; Montréal, QC, Canada.

*Corresponding author. Email: artur.kania@ircm.qc.ca

Summary: Somatotopy is a recurring organisational feature of the somatosensory system where adjacent neurons and their connections represent adjacent regions of the body. The molecular mechanisms governing the formation of such “body maps” remain largely unknown. Here we demonstrate that the cell surface proteins teneurin-3 and latrophilin-2 are expressed in opposing gradients aligning with the somatotopic map in the dorsal horn of the mouse spinal cord. Genetic manipulation of these proteins in spinal dorsal horn or sensory neurons distorts the somatotopy of neuronal connections and impairs accurate localisation of a noxious stimulus on the surface of the body. Our work provides the foundation for a molecular model of somatotopic map formation and insights into the role of somatotopic maps in the ability to accurately locate somatosensory stimuli or topognosis.

Main Text:

Introduction

The architecture of neuronal connections reflects their functional logic. A key organisational feature of neuronal circuits are "topographic maps" that maintain the spatial relationship between a group of neurons and their post-synaptic targets. The consequence of this, in the context of sensory processing, is that information concerning adjacent stimuli is communicated by adjacent neurons at multiple relay nodes of a sensory system. The classical paradigm for studying the development of such organisation are retinotopic maps whose connectivity is driven by gradients of cell surface proteins and refined by cellular-level processes[1–7]. However, knowledge of the molecules that wire other sensory maps, particularly those in the somatosensory system, remains limited.

Somatotopic maps are a unique example of topographic maps where nearby neurons represent contiguous anatomical structures. Somatotopic organisation is characteristic of most vertebrate somatosensory circuits, including the dorsal horn of the spinal cord (DH)[8–10], ventrobasal thalamus[11,12], and primary somatosensory cortex[13,14]. The rodent DH exhibits a mediolateral (ML) organisation that corresponds to the proximodistal (PD) axis of the body, where the medial DH receives sensory inputs from distal regions (e.g. the paw), while the lateral DH corresponds to more proximal regions of the body (e.g. the shoulder/hip to midline)[8–10]. This organisation is also reflected by neuronal activity within the DH induced by sensory stimuli[15–17]. The ML map is oriented orthogonally to the DH laminae that receive modality-specific sensory inputs[18,19]; the result is a columnar-like architecture where a vertical "columel" processes noxious, thermal, and light touch information originating in a particular location on the surface of the body[16,20].

Despite the discovery of somatotopic maps over a century ago, the mechanisms that underlie their development remain poorly understood and their precise role in internal representation of our bodies is speculative[13,21–23]. It is known that neuronal activity plays a critical role in the refinement of developing body maps[24–26]. On the other hand, sensory axons are somatotopically sorted immediately upon entry into the DH, suggesting a contribution by hard-wiring molecular signals[27–31]. However, the identity of these has remained elusive: none of the classical neuronal connectivity molecules appear to be involved despite their extensive study. Here, we identify cell surface proteins teneurin-3 (Ten3) and latrophilin-2 (Lphn2) as essential for the formation of the DH somatotopic map and provide evidence that its miswiring attenuates the accuracy of somatosensory stimulus localisation.

Ten3 and Lphn2 expression reflects the ST organisation of the DH

Recent work has shown that heterophilic repulsion mediated by Ten3 and Lphn2, in combination with Ten3-Ten3 homophilic attraction, establish a point-to-point topography of neuronal connections in the hippocampus[32–34]. To determine whether Lphn2 and Ten3 could direct the development of DH connectivity, we examined their expression in the mouse lumbosacral DH at embryonic day (e) 14.5, when cutaneous afferents begin their entry into spinal laminae I-IV[35,36]. We observed complementary mRNA gradients that spanned the limb somatotopic map: *Lphn2* mRNA expression was high in the medial DH (representing the distal limb) and low in the lateral DH, whereas *Ten3* mRNA expression was high in the lateral DH (representing the proximal limb) and low in the medial DH (Figure 1A). Analysis of protein expression using an anti-Ten3 antibody [32] and *Lphn2-mVenus* knock-in mice[37] revealed similar mediolateral gradients (Figure 1B).

We then examined the afferent inputs to the DH: the primary sensory neurons residing within the dorsal root ganglia (DRG). Although there is no apparent somatotopic organisation of DRG neurons within individual ganglia, different ganglia innervate distinct regions of skin termed "dermatomes"[8,38,39]. Correspondingly, we did not observe any spatial bias to *Ten3* or *Lphn2* expression in individual ganglia along either the dorsoventral or mediolateral axes (Figure S1A). Meanwhile, we did observe an inverse relationship between *Ten3* and *Lphn2* mRNA levels in individual DRG neurons, where those that expressed high levels of *Ten3* also expressed low levels of *Lphn2* and vice versa (Figure S1B). Additionally, DRG neurons that predominantly express either *Ten3* or *Lphn2* could be identified across all major sensory neuron subtypes (Figure S1C).

Reflecting the dermatome organisation, ganglia enriched in distal hindpaw-innervating neurons (L3-L5) had high *Lphn2* and low *Ten3* levels of mRNA. Conversely, ganglia enriched in more proximally-projecting neurons (L1-2 and L6) had low *Lphn2* and high *Ten3* (Figure 1C). Thus, the sensory neuron expression of *Lphn2* and *Ten3* correlated with DH Lphn2 and Ten3 gradients and the somatotopic map of limb: distal limb sensory neurons that innervate the Lphn2-high medial DH express high levels of *Lphn2*, and proximal sensory neurons that innervate the Ten3-high lateral DH express high levels of *Ten3*. A similar correlation could be made between the protein gradients in the DRG axons located in the dorsal root entry zone (DREZ) immediately outside the DH and the gradients in the DH (Figure 1B, quantified in Figure S1D). Next, to determine if Ten3 and Lphn2 gradients align with somatotopic maps in other somatosensory regions, we examined *Ten3* and *Lphn2* mRNA expression in the ventrobasal (VB) thalamus, an important node in the ascending somatosensory pathway, and uncovered a similar gradient that aligned with the VB somatotopic map[11] (Figure S1E). Finally, to examine whether such Ten3/Lphn2 gradients are evolutionarily conserved we examined the expression of *TENM3* and

101 *ADGRL2* mRNAs, which encode the human homologues of mouse Ten3 and Lphn2, in the
102 human fetal dorsal horn and observed similar mediolateral gradients (Figure S1F). Thus, our
103 observations suggest that Ten3 and Lphn2 are expressed in gradients along the proximodistal
104 axis of somatotopic maps in a conserved manner across the somatosensory system.

105

106 **Ten3 and Lphn2 are required for the somatotopic organisation of sensory afferents**

107 Based on the observed expression patterns in the DH and DRG, as well as the previously
108 described functions of these proteins[33], we hypothesized the following: (1) repulsion from Ten3
109 in the DH acting on Lphn2 in DRG axons directs distal limb afferents to the medial DH (Figure
110 1D, left), (2) a combination of repulsion from Lphn2 in the medial DH acting on Ten3 in the
111 DRG axons and attraction from Ten3 in the lateral DH acting on Ten3 in DRG axons cooperate
112 to direct proximal limb afferents to the lateral DH (Figure 1D, right). To test our hypothesis, we
113 first challenged DRG axons with purified $Lphn2^{Lec}$ (the teneurin-binding lectin domain of
114 Lphn2) and the Ten3 extracellular domain. We found that both $Lphn2^{Lec}$ and Ten3 repel DRG
115 axons *in vitro* (Figure S2), thereby demonstrating that Ten3 and Lphn2 can guide DRG axons *in*
116 *vitro*. Next, we generated conditional knockouts (cKOs) of *Ten3* and *Lphn2* in the DRG and DH
117 (Figure S3A; see methods), hereby referred to as $Ten3^{\Delta DRG}$, $Lphn2^{\Delta DRG}$, $Ten3^{\Delta DH}$, and $Lphn2^{\Delta DH}$.
118 To assess the distribution of sensory afferents along the mediolateral extent of the DH, we co-
119 injected cholera toxin subunit B (CTB) and wheat germ agglutinin (WGA) subcutaneously to the
120 hindpaw or dorsal midline. These preferentially label myelinated (e.g. innocuous touch-relaying)
121 and unmyelinated (e.g. pain and temperature-relaying) sensory afferents, respectively[10,26,40].

122 First, we examined distal limb afferent inputs to the DH, which we hypothesized to be
123 guided by Ten3 (DH) → Lphn2 (DRG) repulsion (Figure 1D, left). We examined these afferents

124 in Ten3$^{\Delta DH}$ and Lphn2$^{\Delta DRG}$ cKO mice and littermate controls by injecting CTB/WGA into the
125 hindpaw and quantified the distribution of the labelled axons along the ML and superficial-deep
126 (SD) axes of the DH (Figure S3B; see methods). In wild-type mice, the paw representation is
127 disproportionally large and duplicated at the most medial extreme of the dorsal horn[10,16,26,41]. In
128 our controls, we saw the expected wild-type distribution of afferents, however in Ten3$^{\Delta DH}$ cKO
129 mice we observed a dramatic shift in the ML distribution of labelled afferents (Figures 2A-C and
130 S3C). Despite the shift in ML position, CTB and WGA-labelled axons remained closely aligned
131 with each other along the ML axis (Figure S3D), and there was no shift in the distribution of
132 CTB and WGA-labelled axons along the orthogonal SD axis (Figures S3E-S3G). The
133 Lphn2$^{\Delta DRG}$ cKO mice exhibited a milder but significant shift along the ML axis and no change in
134 the SD axis distribution or in the ML alignment between CTB and WGA-labelled afferents
135 (Figures 2D-F and S3H-L).

136 Next, we examined proximal afferent inputs to the DH, which we hypothesized to be
137 guided by a combination of Lphn2 (DH) → Ten3 (DRG) repulsion and Ten3 (DH) → Ten3
138 (DRG) attraction (Figure 1D, right). We therefore examined these afferents in Ten3$^{\Delta DH}$,
139 Lphn2$^{\Delta DH}$, and Ten3$^{\Delta DRG}$ cKO mice and compared them to littermate controls by injecting
140 CTB/WGA subcutaneously at the dorsal midline. Like for the distal limb afferents, we observed
141 a dramatic shift in the ML distribution of proximal afferents in the Ten3$^{\Delta DH}$ cKO mice (Figures
142 3A-C and S4A). However, this was accompanied by a decrease in the ML alignment of the CTB
143 with the WGA-labelled afferents (Figure S4B), and an expansion in the SD distribution of both
144 classes of afferents (Figures S4C-S4E). Lphn2$^{\Delta DH}$ cKO mice exhibited a comparatively mild but
145 significant shift along the ML and SD axes, without a consequence on the alignment of CTB
146 with the WGA-labelled afferents (Figures 3D-F and S4F-J). Unexpectedly, the Ten3$^{\Delta DRG}$ cKO
147 mice did not exhibit any significant changes in the targeting of afferents in the DH (Figures 3G-I

148 and S4K-O), indicating that Ten3 in the DRG may be dispensable for correct somatotopic and
149 laminar targeting. Importantly, Ten3 (DH) → Lphn2 (DRG) repulsion is likely intact in Ten3$^{\Delta DRG}$
150 cKO mice, suggesting that this repulsion alone may be sufficient to separate the distal and
151 proximal inputs along the ML axis. Together, our cKO experiments demonstrate that Ten3 and
152 Lphn2 are essential for the correct somatotopic organisation of primary sensory afferents in the
153 DH, with the severity of miswiring phenotypes depending on the gene deleted and the targeted
154 tissue.

155

156 **Computational modelling of somatotopic map formation in the DH**

157 To interpret the observed phenotypes and gain further insights into the developmental programs
158 that produce the DH somatotopic map, we constructed a comprehensive computational model of
159 DH somatotopic map formation. Over the past 40 years, several computational models of
160 topographic map formation in the visual system have been developed and iteratively improved.
161 We first determined if these theoretical models of topographic map formation could be applied to
162 somatotopic maps. We therefore adapted the Koulakov model[7,42,43] (see methods) as it is a
163 relatively abstract model without excessive constraints regarding the cellular mechanisms. It also
164 effectively predicts the observed effects of genetic manipulations[44], and incorporates guidance
165 cues, competition, and activity-dependent refinement into a single unified model[7]. After adapting
166 this model to the DH somatotopic map, we then performed Bayesian Simulation-Based Inference
167 (SBI) using the Sequential Monte Carlo method for Approximate Bayesian Computation (ABC-
168 SMC) to identify parameter values for our model that fit both the observed control and cKO data
169 in an unbiased manner (Figure 4A; see methods).

Using the parameter values fit above, we first confirmed that this model was able to accurately reproduce the proximal → lateral and distal → medial connectivity between DRG and DH neurons under wild-type conditions (Figures 4B and S5A). We then confirmed that we were able to closely recapitulate the observed distributions of CTB/WGA along the ML axis in both controls and all cKOs examined experimentally above (Figure 4C). Inspection of the parameter values (table S1) revealed that the best fitting model incorporates a prominent role for activity-dependent refinement of connectivity, consistent with previous observations[24–26]. Furthermore, disrupting activity dependent refinement in our model produced a broadening of DRG axon terminal zones and disruptions to DH somatotopy that was qualitatively similar to experimental observations (Figures S5B-D), validating this component of the model. Our model also indicates that there is strong competition between DRG axons for DH space along the ML axis, consistent with previous results showing an expansion of the saphenous nerve afferent termini when the afferents of the sciatic nerve are eliminated[45,46]. We recreated this experiment *in silico* by ablating proximal limb DRG neurons and observed a similar expansion of the remaining axons to fill the available ML extent of the DH (Figures S5E and S5F), further validating our model. Additional inferences of our model are that Ten3 (DH) → Lphn2 (DRG) repulsion plays a more prominent role than Lphn2 (DH) → Ten3 (DRG) repulsion or Ten3 (DH) → Ten3 (DRG) attraction, and that the loss of Lphn2 or Ten3 likely impacts both guidance and activity-dependent refinement, particularly in the Ten3$^{\Delta DH}$ cKOs. Taken together, we show that despite being developed for a different sensory system patterned by gradients of unrelated molecular cues, a theoretical model of topographic map formation in the visual system can be adapted to accurately represent the developing somatotopic map in the DH.

193 **Ten3$^{\Delta DH}$ cKOs exhibit an altered somatotopic distribution of neural activity and**
194 **behavioural responses**

195 Given the observed miswiring phenotypes, we asked if this miswiring was accompanied by
196 alterations in the function of the DH neuronal circuitry. Towards this end, we selected the cKO
197 with the most severe miswiring phenotype (Ten3$^{\Delta DH}$) and examined the consequence of injecting
198 the hindpaw with formalin, a noxious stimulus that results in a somatotopically restricted
199 induction of the neuronal activity marker c-Fos in DH neurons[15]. Following injection of formalin
200 into the distal hindpaw, both cKO mice and control littermates displayed a significant induction
201 of c-Fos in the DH ipsilateral to the injection (Figures S6A and S6B). While controls showed
202 increased c-Fos expression predominantly in the somatotopically appropriate medial DH,
203 Ten3$^{\Delta DH}$ cKO mice exhibited a greater number of c-Fos-expressing cells in the lateral DH
204 (Figures 5A-D). Matching the more widespread induction of c-Fos, cKO mice also had more c-
205 Fos-expressing cells on the side ipsilateral to the injection when compared to control littermates
206 (Figures S6C-S6E).

207 In addition to being able to induce somatotopically restricted c-Fos activity, formalin
208 injection elicits highly accurate licking of the injection site. Thus, using this paradigm we sought
209 to examine the functional impact of somatotopic miswiring on the ability to locate a stimulus on
210 the surface of the body, or topognosis. We first examined the precision of topognosis in Ten3
211 constitutive knockout (Ten3^{KO}) mice[32,47]. Compared to control littermates, Ten3^{KO} mice spent
212 less time licking regions of the limb close to the injection site and more time licking regions of
213 the limb farther from the injection (Figures 6F and G), potentially indicating a deficit in their
214 ability to precisely locate the stimulus. Meanwhile, the total duration of licking, an indication of
215 stimulus intensity, was not different between KO and control mice (Figure 6H). However,

216 Ten3^{KO} mice also showed defects in the ability to remove an adhesive tape placed on their
217 hindlimbs, suggesting broad deficits in sensorimotor coordination (Figures S6I and S6J).

218 We next assessed topognosis in Ten3$^{\Delta DH}$ cKO mice given the magnitude of their anatomical
219 miswiring phenotype. Similar to the Ten3^{KO} mice, Ten3$^{\Delta DH}$ cKO mice exhibited a reduction in
220 time spent licking areas close to the injection and increase in time licking areas farther from the
221 injection site (Figures 5E and S6K), indicating impaired topognosis. This phenotype was not
222 accompanied by any significant changes in total licking duration (Figure S6L). Finally, unlike
223 the Ten3^{KO} mice, Ten3$^{\Delta DH}$ mice performed normally in the adhesive removal assay (Figures S6M
224 and S6N), indicating normal sensorimotor coordination. Together, these data indicate that loss of
225 Ten3 in the DH, in addition to causing significant disruptions to DH somatotopy, impairs
226 somatosensory topognosis.

227

228 **Discussion**

229 Our study provides foundational insights into the molecular logic of somatotopic map formation.
230 First, our experimental observations and modelling argue that the somatotopic map formed
231 between peripheral sensory neurons and those in the spinal DH is driven by graded expression of
232 Ten3 and Lphn2. This complements previous studies on their role in establishing of neuronal
233 connections through binary or all-or-nothing attractive and repulsive signalling. Additionally, we
234 also provide direct functional evidence of the importance of somatotopic maps in the ability to
235 localise a stimulus on the surface of the body.

236 Several parallels and distinctions between our work and that on the formation of retinotopic
237 maps can be made. Like in retinotopic maps, past studies and this work suggest that axon-axon
238 interactions such as pre-ordering prior to arrival in target area and inter-axon competition, as well

239 as activity-dependent refinement, play an important role in the establishment of the DH
240 somatotopic map. However, while disrupting EphA/ephrin-A signalling largely results in the
241 formation of additional discrete terminal zones of retinal axons in the superior colliculus[5], we
242 generally observe broadening and/or shifting of sensory axon terminal zones in the ML axis of
243 the DH, without the formation of additional ones, suggesting fundamental cellular/molecular
244 differences between these processes. Of particular interest would be the significance of
245 Ten3/Lphn2 and EphA/ephrin-A co-expression, the latter of which have been implicated in
246 somatosensory cortex somatotopic map formation by specifying afferent thalamic axon
247 connectivity[48,49]. Finally, the presence of Ten3/Lphn2 gradients in many regions of the
248 developing nervous system raises the possibility that they pattern all somatotopic maps within
249 the somatosensory system, and more generally, circuits whose organising principle requires the
250 preservation of spatial relationship between neurons and their targets[50].

251 Although we cannot rule out other DH functions of Ten3 contributing to the impaired topognosis
252 phenotype, to our knowledge, our data represent the only functional evidence indicating a
253 requirement for somatotopic maps in topognosis. More generally, our data adds to the currently
254 limited behavioural evidence that topographic maps are required for correct sensory processing.
255 Finally, the unchanged duration of licking in response to formalin in Ten3$^{\Delta DH}$ cKOs suggests that
256 stimulus intensity and location can be dissociated, echoing the idea of parallel
257 motivational/affective and discriminatory systems underlying nociception[51]. Our genetics-based
258 precise manipulation of a somatotopic map provides a new inroad into questions such as body
259 map plasticity, the integration of somatotopic somatosensory maps with somatotopic motor
260 maps, or those of other sensory modalities, and their overall function in representing our bodies
261 and whole-body action planning[23].

References and Notes

1. Sperry, R.W. (1963). Chemoaffinity in the orderly growth of nerve fiber patterns and connections*. Proceedings of the National Academy of Sciences *50*, 703–710. https://doi.org/10.1073/pnas.50.4.703.

2. Cheng, H.-J., Nakamoto, M., Bergemann, A.D., and Flanagan, J.G. (1995). Complementary gradients in expression and binding of ELF-1 and Mek4 in development of the topographic retinotectal projection map. Cell *82*, 371–381. https://doi.org/10.1016/0092-8674(95)90426-3.

3. Drescher, U., Kremoser, C., Handwerker, C., Löschinger, J., Noda, M., and Bonhoeffer, F. (1995). In vitro guidance of retinal ganglion cell axons by RAGS, a 25 kDa tectal protein related to ligands for Eph receptor tyrosine kinases. Cell *82*, 359–370. https://doi.org/10.1016/0092-8674(95)90425-5.

4. Cline, H.T., and Constantine-Paton, M. (1989). NMDA receptor antagonists disrupt the retinotectal topographic map. Neuron *3*, 413–426. https://doi.org/10.1016/0896-6273(89)90201-8.

5. Feldheim, D.A., Kim, Y.-I., Bergemann, A.D., Frisén, J., Barbacid, M., and Flanagan, J.G. (2000). Genetic Analysis of Ephrin-A2 and Ephrin-A5 Shows Their Requirement in Multiple Aspects of Retinocollicular Mapping. Neuron *25*, 563–574. https://doi.org/10.1016/S0896-6273(00)81060-0.

6. Rashid, T., Upton, A.L., Blentic, A., Ciossek, T., Knöll, B., Thompson, I.D., and Drescher, U. (2005). Opposing Gradients of Ephrin-As and EphA7 in the Superior Colliculus Are Essential for Topographic Mapping in the Mammalian Visual System. Neuron *47*, 57–69. https://doi.org/10.1016/j.neuron.2005.05.030.

7. Triplett, J.W., Pfeiffenberger, C., Yamada, J., Stafford, B.K., Sweeney, N.T., Litke, A.M., Sher, A., Koulakov, A.A., and Feldheim, D.A. (2011). Competition is a driving force in topographic mapping. Proceedings of the National Academy of Sciences *108*, 19060–19065. https://doi.org/10.1073/pnas.1102834108.

8. Grant, G., and Ygge, J. (1981). Somatotopic organization of the thoracic spinal nerve in the dorsal horn demonstrated with transganglionic degeneration. Journal of Comparative Neurology *202*, 357–364. https://doi.org/10.1002/cne.902020305.

9. Takahashi, Y., Chiba, T., Kurokawa, M., and Aoki, Y. (2003). Dermatomes and the central organization of dermatomes and body surface regions in the spinal cord dorsal horn in rats. Journal of Comparative Neurology *462*, 29–41. https://doi.org/10.1002/cne.10669.

10. Odagaki, K., Kameda, H., Hayashi, T., and Sakurai, M. (2019). Mediolateral and dorsoventral projection patterns of cutaneous afferents within transverse planes of the mouse spinal dorsal horn. Journal of Comparative Neurology *527*, 972–984. https://doi.org/10.1002/cne.24593.

11. Francis, J.T., Xu, S., and Chapin, J.K. (2008). Proprioceptive and Cutaneous Representations in the Rat Ventral Posterolateral Thalamus. Journal of Neurophysiology *99*, 2291–2304. https://doi.org/10.1152/jn.01206.2007.

12. Tasker, R.R., Organ, L.W., and Hawrylyshyn, P. (1976). Sensory Organization of the Human Thalamus. Applied Neurophysiology *39*, 139–153. https://doi.org/10.1159/000102487.

13. Penfield, W., and Boldrey, E. (1937). Somatic motor and sensory representation in the cerebral cortex of man as studied by electrical stimulation. Brain *60*, 389–443. https://doi.org/10.1093/brain/60.4.389.

14. Ebner, F.F., and Kaas, J.H. (2015). Chapter 24 - Somatosensory System. In The Rat Nervous System (Fourth Edition), G. Paxinos, ed. (Academic Press), pp. 675–701. https://doi.org/10.1016/B978-0-12-374245-2.00024-3.

15. Bullitt, E. (1991). Somatotopy of spinal nociceptive processing. Journal of Comparative Neurology *312*, 279–290. https://doi.org/10.1002/cne.903120210.

16. Levinsson, A., Holmberg, H., Broman, J., Zhang, M., and Schouenborg, J. (2002). Spinal Sensorimotor Transformation: Relation between Cutaneous Somatotopy and a Reflex Network. J. Neurosci. *22*, 8170–8182. https://doi.org/10.1523/JNEUROSCI.22-18-08170.2002.

17. Warwick, C., Salsovic, J., Hachisuka, J., Smith, K.M., Sheahan, T.D., Chen, H., Ibinson, J., Koerber, H.R., and Ross, S.E. (2022). Cell type-specific calcium imaging of central sensitization in mouse dorsal horn. Nat Commun *13*, 5199. https://doi.org/10.1038/s41467-022-32608-2.

18. Rexed, B. (1952). The cytoarchitectonic organization of the spinal cord in the cat. Journal of Comparative Neurology *96*, 415–495. https://doi.org/10.1002/cne.900960303.

19. Gatto, G., Bourane, S., Ren, X., Di Costanzo, S., Fenton, P.K., Halder, P., Seal, R.P., and Goulding, M.D. (2021). A Functional Topographic Map for Spinal Sensorimotor Reflexes. Neuron *109*, 91-104.e5. https://doi.org/10.1016/j.neuron.2020.10.003.

20. Willis, W.D., and Coggeshall, R.E. (1991). Sensory Mechanisms of the Spinal Cord (Springer US) https://doi.org/10.1007/978-1-4899-0597-0.

21. Grünbaum, A.S.F., and Sherrington, C.S. (1901). Observations on the physiology of the cerebral cortex of some of the higher apes. (Preliminary communication.). Proceedings of the Royal Society of London *69*, 206–209. https://doi.org/10.1098/rspl.1901.0100.

22. Hassler, R. (2019). New Aspects of Brain Functions Revealed by Brain Diseases. In Frontiers in Brain Research, J. D. French, ed. (Columbia University Press), pp. 242–288.

23. Gordon, E.M., Chauvin, R.J., Van, A.N., Rajesh, A., Nielsen, A., Newbold, D.J., Lynch, C.J., Seider, N.A., Krimmel, S.R., Scheidter, K.M., et al. (2023). A somato-cognitive action network alternates with effector regions in motor cortex. Nature *617*, 351–359. https://doi.org/10.1038/s41586-023-05964-2.

24. Mendelson, B. (1994). Chronic embryonic MK-801 exposure disrupts the somatotopic organization of cutaneous nerve projections in the chick spinal cord. Developmental Brain Research *82*, 152–166. https://doi.org/10.1016/0165-3806(94)90158-9.

25. Beggs, S., Torsney, C., Drew, L.J., and Fitzgerald, M. (2002). The postnatal reorganization of primary afferent input and dorsal horn cell receptive fields in the rat spinal cord is an activity-dependent process. European Journal of Neuroscience *16*, 1249–1258. https://doi.org/10.1046/j.1460-9568.2002.02185.x.

26. Granmo, M., Petersson, P., and Schouenborg, J. (2008). Action-Based Body Maps in the Spinal Cord Emerge from a Transitory Floating Organization. J. Neurosci. *28*, 5494–5503. https://doi.org/10.1523/JNEUROSCI.0651-08.2008.

27. Mirnics, K., and Koerher, H.R. (1995). Prenatal development of rat primary afferent fibers: II. Central projections. Journal of Comparative Neurology *355*, 601–614. https://doi.org/10.1002/cne.903550409.

28. Smith, C.L. (1983). The development and postnatal organization of primary afferent projections to the rat thoracic spinal cord. Journal of Comparative Neurology *220*, 29–43. https://doi.org/10.1002/cne.902200105.

29. Fitzgerald, M. (1987). Prenatal growth of fine-diameter primary afferents into the rat spinal cord: A transganglionic tracer study. Journal of Comparative Neurology *261*, 98–104. https://doi.org/10.1002/cne.902610108.

30. Silos-Santiago, I., Jeng, B., and Snider, W.D. (1995). Sensory afferents show appropriate somatotopy at the earliest stage of projection to dorsal horn: NeuroReport *6*, 861–865. https://doi.org/10.1097/00001756-199504190-00009.

31. Arcaro, M.J., Schade, P.F., and Livingstone, M.S. (2019). Body map proto-organization in newborn macaques. Proceedings of the National Academy of Sciences *116*, 24861–24871. https://doi.org/10.1073/pnas.1912636116.

32. Berns, D.S., DeNardo, L.A., Pederick, D.T., and Luo, L. (2018). Teneurin-3 controls topographic circuit assembly in the hippocampus. Nature *554*, 328–333. https://doi.org/10.1038/nature25463.

33. Pederick, D.T., Lui, J.H., Gingrich, E.C., Xu, C., Wagner, M.J., Liu, Y., He, Z., Quake, S.R., and Luo, L. (2021). Reciprocal repulsions instruct the precise assembly of parallel hippocampal networks. Science *372*, 1068–1073. https://doi.org/10.1126/science.abg1774.

34. Gringrich, E.C., Pederick, D.T., Zhang, Y., and Luo, L. (2025). Ten3–Lphn2-mediated target selection across the extended hippocampal network demonstrates a repeated strategy for circuit assembly. Preprint at bioRxiv, https://doi.org/10.1101/2025.08.13.670207 https://doi.org/10.1101/2025.08.13.670207.

35. Ozaki, S., and Snider, W.D. (1997). Initial trajectories of sensory axons toward laminar targets in the developing mouse spinal cord. Journal of Comparative Neurology *380*, 215–229. https://doi.org/10.1002/(SICI)1096-9861(19970407)380:2<215::AID-CNE5>3.0.CO;2-6.

36. Hasegawa, H., Abbott, S., Han, B.-X., Qi, Y., and Wang, F. (2007). Analyzing Somatosensory Axon Projections with the Sensory Neuron-Specific Advillin Gene. J. Neurosci. *27*, 14404–14414. https://doi.org/10.1523/JNEUROSCI.4908-07.2007.

37. Anderson, G.R., Maxeiner, S., Sando, R., Tsetsenis, T., Malenka, R.C., and Südhof, T.C. (2017). Postsynaptic adhesion GPCR latrophilin-2 mediates target recognition in entorhinal-hippocampal synapse assembly. Journal of Cell Biology *216*, 3831–3846. https://doi.org/10.1083/jcb.201703042.

38. Molander, C., and Grant, G. (1985). Cutaneous projections from the rat hindlimb foot to the substantia gelatinosa of the spinal cord studied by transganglionic transport of WGA-HRP conjugate. Journal of Comparative Neurology *237*, 476–484. https://doi.org/10.1002/cne.902370405.

39. Prats-Galino, A., Puigdellívol-sánchez, A., Ruano-Gil, D., and Molander, C. (1999). Representations of hindlimb digits in rat dorsal root ganglia. Journal of Comparative Neurology *408*, 137–145. https://doi.org/10.1002/(SICI)1096-9861(19990524)408:1<137::AID-CNE10>3.0.CO;2-3.

40. Maslany, S., Crockett, D.P., and David Egger, M. (1992). Organization of cutaneous primary afferent fibers projecting to the dorsal horn in the rat: WGA-HRP versus B-HRP. Brain Research *569*, 123–135. https://doi.org/10.1016/0006-8993(92)90378-M.

41. Swett, J.E., and Woolf, C.J. (1985). The somatotopic organization of primary afferent terminals in the superficial laminae of the dorsal horn of the rat spinal cord. Journal of Comparative Neurology *231*, 66–77. https://doi.org/10.1002/cne.902310106.

42. Koulakov, A.A., and Tsigankov, D.N. (2004). A stochastic model for retinocollicular map development. BMC Neurosci *5*, 30. https://doi.org/10.1186/1471-2202-5-30.

43. Tsigankov, D.N., and Koulakov, A.A. (2006). A unifying model for activity-dependent and activity-independent mechanisms predicts complete structure of topographic maps in ephrin-A deficient mice. J Comput Neurosci *21*, 101–114. https://doi.org/10.1007/s10827-006-9575-7.

44. Hjorth, J.J.J., Sterratt, D.C., Cutts, C.S., Willshaw, D.J., and Eglen, S.J. (2015). Quantitative assessment of computational models for retinotopic map formation. Developmental Neurobiology *75*, 641–666. https://doi.org/10.1002/dneu.22241.

45. Fitzgerald, M. (1985). The sprouting of saphenous nerve terminals in the spinal cord following early postnatal sciatic nerve section in the rat. Journal of Comparative Neurology *240*, 407–413. https://doi.org/10.1002/cne.902400408.

46. Fitzgerald, M., Woolf, C.J., and Shortland, P. (1990). Collateral sprouting of the central terminals of cutaneous primary afferent neurons in the rat spinal cord: Pattern, morphology, and influence of targets. Journal of Comparative Neurology *300*, 370–385. https://doi.org/10.1002/cne.903000308.

47. Leamey, C.A., Merlin, S., Lattouf, P., Sawatari, A., Zhou, X., Demel, N., Glendining, K.A., Oohashi, T., Sur, M., and Fässler, R. (2007). Ten_m3 Regulates Eye-Specific Patterning in the

Mammalian Visual Pathway and Is Required for Binocular Vision. PLOS Biology *5*, e241. https://doi.org/10.1371/journal.pbio.0050241.

48. Vanderhaeghen, P., Lu, Q., Prakash, N., Frisén, J., Walsh, C.A., Frostig, R.D., and Flanagan, J.G. (2000). A mapping label required for normal scale of body representation in the cortex. Nat Neurosci *3*, 358–365. https://doi.org/10.1038/73929.

49. Dufour, A., Seibt, J., Passante, L., Depaepe, V., Ciossek, T., Frisén, J., Kullander, K., Flanagan, J.G., Polleux, F., and Vanderhaeghen, P. (2003). Area Specificity and Topography of Thalamocortical Projections Are Controlled by ephrin/Eph Genes. Neuron *39*, 453–465. https://doi.org/10.1016/S0896-6273(03)00440-9.

50. Chon, U., Pederick, D.T., Song, J.H., Zhang, Y., Rana, I., and Luo, L. (2025). Inverse expression of Ten3 and Lphn2 across the developing mouse brain reveals a global strategy for circuit assembly. Preprint at bioRxiv, https://doi.org/10.1101/2025.08.13.670004 https://doi.org/10.1101/2025.08.13.670004.

51. Melzack, R., and Casey, K. (1968). Sensory, motivational, and central control determinants of pain. Kenshalo DR, editor. The skin senses: proceedings. Springfield (Illinois): Charles C. Thomas, 423–443.

52. Sieber, M.A., Storm, R., Martinez-de-la-Torre, M., Müller, T., Wende, H., Reuter, K., Vasyutina, E., and Birchmeier, C. (2007). Lbx1 Acts as a Selector Gene in the Fate Determination of Somatosensory and Viscerosensory Relay Neurons in the Hindbrain. J. Neurosci. *27*, 4902–4909. https://doi.org/10.1523/JNEUROSCI.0717-07.2007.

53. Pietri, T., Eder, O., Blanche, M., Thiery, J.P., and Dufour, S. (2003). The human tissue plasminogen activator-Cre mouse: a new tool for targeting specifically neural crest cells and their derivatives in vivo. Developmental Biology *259*, 176–187. https://doi.org/10.1016/S0012-1606(03)00175-1.

54. Lai, H.C., Seal, R.P., and Johnson, J.E. (2016). Making sense out of spinal cord somatosensory development. Development *143*, 3434–3448. https://doi.org/10.1242/dev.139592.

55. Müller, T., Brohmann, H., Pierani, A., Heppenstall, P.A., Lewin, G.R., Jessell, T.M., and Birchmeier, C. (2002). The Homeodomain Factor Lbx1 Distinguishes Two Major Programs of Neuronal Differentiation in the Dorsal Spinal Cord. Neuron *34*, 551–562. https://doi.org/10.1016/S0896-6273(02)00689-X.

56. Paixão, S., Balijepalli, A., Serradj, N., Niu, J., Luo, W., Martin, J.H., and Klein, R. (2013). EphrinB3/EphA4-Mediated Guidance of Ascending and Descending Spinal Tracts. Neuron *80*, 1407–1420. https://doi.org/10.1016/j.neuron.2013.10.006.

57. Bouet, V., Boulouard, M., Toutain, J., Divoux, D., Bernaudin, M., Schumann-Bard, P., and Freret, T. (2009). The adhesive removal test: a sensitive method to assess sensorimotor deficits in mice. Nat Protoc *4*, 1560–1564. https://doi.org/10.1038/nprot.2009.125.

58. Roome, R.B., Bourojeni, F.B., Mona, B., Rastegar-Pouyani, S., Blain, R., Dumouchel, A., Salesse, C., Thompson, W.S., Brookbank, M., Gitton, Y., et al. (2020). Phox2a Defines a Developmental

Origin of the Anterolateral System in Mice and Humans. Cell Reports *33*, 108425. https://doi.org/10.1016/j.celrep.2020.108425.

59. Hunskaar, S., and Hole, K. (1987). The formalin test in mice: dissociation between inflammatory and non-inflammatory pain. Pain *30*, 103–114. https://doi.org/10.1016/0304-3959(87)90088-1.

60. Mogil, J.S., Wilson, S.G., Bon, K., Eun Lee, S., Chung, K., Raber, P., Pieper, J.O., Hain, H.S., Belknap, J.K., Hubert, L., et al. (1999). Heritability of nociception I: Responses of 11 inbred mouse strains on 12 measures of nociception. Pain *80*, 67–82. https://doi.org/10.1016/S0304-3959(98)00197-3.

61. del Toro, D., Carrasquero-Ordaz, M.A., Chu, A., Ruff, T., Shahin, M., Jackson, V.A., Chavent, M., Berbeira-Santana, M., Seyit-Bremer, G., Brignani, S., et al. (2020). Structural Basis of Teneurin-Latrophilin Interaction in Repulsive Guidance of Migrating Neurons. Cell *180*, 323-339.e19. https://doi.org/10.1016/j.cell.2019.12.014.

62. Schneider, C.A., Rasband, W.S., and Eliceiri, K.W. (2012). NIH Image to ImageJ: 25 years of image analysis. Nat Methods *9*, 671–675. https://doi.org/10.1038/nmeth.2089.

63. Bankhead, P., Loughrey, M.B., Fernández, J.A., Dombrowski, Y., McArt, D.G., Dunne, P.D., McQuaid, S., Gray, R.T., Murray, L.J., Coleman, H.G., et al. (2017). QuPath: Open source software for digital pathology image analysis. Sci Rep *7*, 16878. https://doi.org/10.1038/s41598-017-17204-5.

64. Schmidt, U., Weigert, M., Broaddus, C., and Myers, G. (2018). Cell Detection with Star-Convex Polygons. In Medical Image Computing and Computer Assisted Intervention – MICCAI 2018 Lecture Notes in Computer Science., A. F. Frangi, J. A. Schnabel, C. Davatzikos, C. Alberola-López, and G. Fichtinger, eds. (Springer International Publishing), pp. 265–273. https://doi.org/10.1007/978-3-030-00934-2_30.

65. R Core Team (2021). R: A Language and Environment for Statistical Computing (R Foundation for Statistical Computing).

66. Schindelin, J., Arganda-Carreras, I., Frise, E., Kaynig, V., Longair, M., Pietzsch, T., Preibisch, S., Rueden, C., Saalfeld, S., Schmid, B., et al. (2012). Fiji: an open-source platform for biological-image analysis. Nat Methods *9*, 676–682. https://doi.org/10.1038/nmeth.2019.

67. Südhof, T.C. (2025). Signaling by latrophilin adhesion-GPCRs in synapse assembly. Neuroscience. https://doi.org/10.1016/j.neuroscience.2025.03.041.

68. Sisson, S.A., Fan, Y., and Beaumont, M. (2018). Handbook of Approximate Bayesian Computation (CRC Press).

69. Schälte, Y., Klinger, E., Alamoudi, E., and Hasenauer, J. (2022). pyABC: Efficient and robust easy-to-use approximate Bayesian computation. Journal of Open Source Software *7*, 4304. https://doi.org/10.21105/joss.04304.

70. Wickham, H. (2016). ggplot2: Elegant Graphics for Data Analysis (Springer-Verlag New York).

71. Kassambara, A. (2022). rstatix: Pipe-Friendly Framework for Basic Statistical Tests.

484

Methods

Acquisition of human tissue

Collection of the human fetal spinal cord samples were obtained with the parents' written informed consent through a spontaneous or induced abortion donor program at the Centre hospitalier universitaire - Sainte-Justine (CHU-SJ), approved by the IRCM and CHU-SJ Research Ethics Committee under the name "Pour une meilleure compréhension du développement de la moelle épinière et des maladies qui y sont associées". Donor spinal cords were dissected and fixed for 24h in formalin, then processed for cryosectioning as below.

Mouse lines

All animal studies were approved by the IRCM's Animal Care Committee in agreement with Canadian Council on Animal Care (CCAC) guidelines, as per protocol numbers 2021-12AK and 2023-11AK. Mice were group-housed with access to food and water *ad libitum*. All mice were maintained on a mixed C57BL/6 and 129/Sv background and both male and female mice were used in all experiments. Mouse lines used in this study include *Lbx1:Cre*[52], *PLAT:Cre*[53], *Ten3*$^{fl(32)}$, *Lphn2*$^{fl(37)}$, *Lphn2-mVenus*[37], and *Ten3*$^{KO(47)}$. Within the spinal cord, *Lbx1:Cre* drives recombination within the dI4/dILA, dI5/dILB neurons which make up the majority of the DH while sparing most other spinal populations and the DRG[54–56]. *PLAT:cre* is expressed in neural crest derived cells, including DRG neurons, while sparing the spinal cord and brain[53]. *PLAT:Cre* was chosen over alternatives like *Pirt:Cre* and *Advilin:Cre* since these are expressed in neural crest-derived cells as early as Theiler Stage 15 (e9.5) and throughout DRG neurons by e11.5 (Figure S2A).

507

508 **Cutaneous CTB/WGA injections**

509 Adult mice (>8 weeks old) were anaesthetised via continuous inhalation of isofluorane (1-3%)
510 and injected with 4 µL of a mixture of 5 mg/mL CTB-AF488 (Thermo Fisher Scientific , cat.
511 #C34775) and 20 mg/mL WGA-AF555 (Thermo Fisher Scientific , cat. #W32464) dissolved in
512 sterile PBS. Blunt forceps were used to pinch and stabilize the skin and injections were
513 performed into the dermis using a beveled glass capillary needle. Distal injections were
514 performed to the glabrous skin of the hindpaw between the two distal-most promontories.
515 Proximal injections were performed at the dorsal midline at the same rostrocaudal level as the
516 iliac crest. All mice were perfused after three days following the injection as described below.

517

518 **Adhesive removal assay**

519 The adhesive removal assay was performed as previously described[57,58]. In brief, mice were
520 tested on their ability to remove an adhesive (half of a 1.5 mL Eppendorf tube cap label, cut into
521 a semicircle) placed on the plantar surface of the hindpaw. The assay was repeated for five
522 consecutive days, with the first four days considered training days and only the final day used for
523 comparison. The latency to remove the adhesive was recorded in seconds, with a maximum time
524 of 30 minutes. If mice exceeded the maximum time, it was marked as a "failure to remove" and
525 the latency was recorded as 30 minutes for the purpose of data analysis. Mice then returned to
526 their home cage.

527

528 **Formalin Assay and c-Fos induction**

529 The formalin assay was performed as previously described[58–60]. Mice were first habituated to the
530 testing chamber (a clear plastic cylinder filmed from below). They were then subcutaneously
531 injected with 20 µL of 2% formalin (in 0.9% saline) to the plantar surface of the hind paw using
532 a 28G needle and returned to the chamber. Mice were filmed from below for 60 minutes
533 following injection. All quantification of time spent licking each region of the body was done in
534 the acute phase (0-10 minutes after injection). Mice were then anesthetized and, after an
535 additional 30 minutes, perfused as described below to analyze the distribution of c-Fos protein
536 (after a total of 90 minutes following the stimulus).

537

538 **Tissue fixation, freezing and sectioning**

539 Mice were anesthetized via intraperitoneal injection of a Ketamine/Xylazine mixture (0.1mL/g
540 body weight of 10 mg/mL Ketamine, 1 mg/mL Xyaline, in 0.9% saline). Mice were then
541 perfused with approximately 15 mL of 1x PBS followed by 15 mL of 4% PFA in PBS. Spinal
542 cords were post-fixed in 4% PFA overnight, washed 3x with PBS and left in a 30% sucrose in
543 PBS solution until they had sunk. Tissue was cryosectioned into 25 µm sections for adult tissue
544 used for immunohistochemistry and 12 µm sections for embryonic tissue and adult tissue used
545 for mRNA detection using RNAscope (Advanced Cell Diagnostics (ACDbio)).

546

547 **DRG explant culture on Ten3/Lphn2 stripes**

548 DRG explants from E15.5 embryos were dissected and plated on 6 cm dishes containing stripes,
549 prepared essentially as previously described[61]. Briefly, 100 µg/mL of Fc recombinant protein,
550 Lphn2-Lec or Tenm3, were mixed with Alexa 594-conjugated anti-hFc antibody (Thermo Fisher

551 Scientific, cat. #A-11014) in PBS. Proteins were injected into matrices (90 µm width) and placed
552 on 60 mm dishes, resulting in red fluorescent stripes. After 30 min incubation at 37°C, dishes
553 were washed with PBS and matrices removed. Dishes were coated with 100 µg/mL Fc
554 conjugated with anti-hFc (Jackson ImmunoResearch, cat. #109-001-008) for 30 min at 37°C and
555 washed with PBS. Stripes were further coated with 20 µg/mL Laminin in PBS for at least 2 h and
556 washed with PBS. Explants were then cultured for 1-2 days in vitro at 37°C, 5% CO2 in
557 Neurobasal medium plus B27 supplement with the addition of 20 ng/mL Nerve Growth Factor
558 (NGF) and 10 ng/mL Glial cell line-Derived Neurotrophic Factor (GDNF). Samples were then
559 fixed with 4% paraformaldehyde for 20 minutes and stained with rabbit monoclonal anti-beta-III
560 tubulin antibody (Sigma-Aldrich, cat. #ZRB1140) after 20 min permeabilization in 1% BSA,
561 0.1% Triton X-100 in PBS. Cy2 anti-rabbit IgG secondary antibody (Jackson ImmunoResearch,
562 cat. #111-225-144) was used to detect tubulin. For all conditions $n \geq 15$ DRG explants were
563 used. The numbers of beta-III-tubulin-positive (green) pixels on red or black stripes were
564 quantified with ImageJ (version 1.54p)[62] using a custom-made automatic macro (available upon
565 request).

566

567 **Immunohistochemistry**

568 Tissue sections were washed three times with 1x PBS for 5 minutes, blocked for 30 minutes
569 using a solution of 5% heat-inactivated horse serum (HIHS) and 0.1% Triton X-100 in PBS
570 (0.1% tPBS). They were then incubated primary antibody solution (primary antibody in 1%
571 HIHS, 0.1% tPBS) overnight and washed three times with 1x PBS for 5 minutes before being
572 incubated with a secondary antibody (in 1% HIHS, 0.1% tPBS) for 1 hour at room temperature,
573 washed three more times with 1x PBS for 5 minutes, and counterstained with DAPI (4′,6-

574 diamidino-2-phenylindole, Fisher Scientific, cat. # D1306). Slides were coverslipped using a
575 solution of 10% Mowiol (Sigma) and 25% glycerol, then allowed to dry prior to imaging.
576 Primary antibodies used were Rabbit anti-Ten3[32] (1:500), Goat anti-GFP (1:500, Abcam,
577 ab6673), Mouse anti-NeuN (1:1000, Millipore Sigma, MAB377), Rabbit anti-WGA (1:500,
578 Millipore Sigma, T4144), Goat anti-CTB (1:5000, List Biological Laboratories, #703), Rabbit
579 anti-c-Fos (1:1000, Cell Signaling Technology, #2250S), Goat anti-TrkA (1:500, R&D Systems,
580 AF1056), Goat anti-TrkB (1:500, R&D Systems, AF1494), and Goat anti-TrkC (1:500, R&D
581 Systems, AF373). Donkey secondary antibodies conjugated to Alexa 488, Cy3, or Cy5 were used
582 (1:500, Jackson ImmunoResearch). Micrographs of tissue sections were acquired using the Leica
583 DM6 or SP8 microscopes.

584

585 **RNAscope ISH and analysis**

586 RNAscope *in situ* mRNA detection was performed according to the manufacturer's protocol
587 using the RNAscope multiplex fluorescent reagent kit (ACDbio, cat. #323100). Probes used
588 were Mm-Tenm3-C1 (ACDbio, cat. #411951) and Mm-Lphn2-C2 (ACDbio, cat. #319341-C2).
589 All images of RNAscope-stained sections were acquired using a Leica SP8 confocal microscope.
590 RNAscope images were quantified using QuPath bioimage analysis software (version 0.4.4) [63].
591 Nuclear segmentation was performed using StarDist[64] and individual puncti and clusters were
592 identified using the QuPath subcellular object detection pipeline. Subcellular detection counts
593 associated with individual cells and their associated coordinates were exported from QuPath and
594 analyzed further in R[65] (version 4.0.5). The x coordinate location of each cell (mediolateral
595 position) was remapped to a 100-unit standard space and counts for a cells within a given area
596 were binned and visualized as mean counts per cell ± one standard error.

CTB and WGA Image analysis

Initial preprocessing of images from CTB/WGA injections was performed using Fiji[66] (version 2.14.0/1.54f). Images were first cropped to the dorsal horn up until lamina V and an outline was manually drawn to indicate the region of interest (ROI). For analyses of both tracers, the two channels were first merged using the imageCalculator "Add" function. Fluorescence intensity from all channels were scaled using "Enhance Contrast" with "saturated=0.1" before being thresholded using the auto threshold method "MaxEntropy dark". Preprocessed images and manually drawn ROIs were then further analyzed in R[65] (version 4.0.5). To account for the curvature of the dorsal horn (with laminae curved downward almost 90 degrees at the lateral extreme), pixel coordinates within each ROI were remapped to a set of anatomical coordinates according to the following functions:

$$f_{ML}(x,y) = \begin{cases} x, & x \leq max(x)/2 \\ \tan^{-1}((x - x_0)/(y - y_0)), & x > max(x)/2 \end{cases}$$

for mapping *x* and *y* pixel coordinates to ML coordinates, and

$$f_{SD}(x,y) = \begin{cases} y, & x \leq max(x)/2 \\ \sqrt[2]{(x - x_0)^2 + (y - y_0)^2}, & x > max(x)/2 \end{cases}$$

616 for mapping x and y pixel coordinates to SD coordinates. Where (x_0, y_0) is the origin, with x_0 set
617 at the midpoint of the ROI and y_0 set at the lamina IV/V border for f_{SD} and the lamina V/VI
618 border for f_{ML}. $Max(x)$ refers to the maximum x coordinate within the ROI and not the whole
619 image. ML and SD coordinates were then normalized to between 0 and 1. Representative
620 examples of these remapped coordinates are provided here (Figure S2B). The DH was then
621 divided into 50 bins along the ML or SD axes and the fluorescence intensity in each bin is
622 represented as a percent of the total signal (such that the values of all bins sum to 100). Since the
623 bins are created based on distance along the given axis, they are not necessarily of equal size
624 (also given the variability of DH anatomy) and therefore the fluorescence intensity is
625 additionally normalized to bin area.

626

627 **c-Fos image analysis**

628 Counts of c-Fos-positive cells was performed manually using the Cell Counter plugin for Fiji[66]
629 (version 2.14.0/1.54f) and xml files containing the coordinates of each marker were exported for
630 further processing in R[65] (version 4.0.5). Marker coordinates were remapped to standardized
631 anatomical coordinates as described above. For the remainder of the analyses, the DH was then
632 divided into 5 bins along the ML or SD axes and the raw unnormalized count of c-Fos positive
633 cells per bin was used.

634

635 **Computational modelling**

636 To adapt the Koulakov model[7,42,43] to the DH ST map, we added parameters governing the
637 strength of Ten3/Lphn2 repulsion/attraction since the original model assumed all

repulsive/attractive interactions to be of equal strength which may not hold in our case. We also reasoned that it was possible for activity-dependent refinement to be disrupted in our cKOs, either due to the synaptic roles of Teneurins and Latrophilins[67], or as a secondary circuit-level consequence of ST miswiring, which might then further contribute to the observed ML distribution shifts. We thus incorporated into our model the ability of cKOs to affect activity-dependent refinement and added additional parameters to govern how this interaction occurs, if at all. These parameters determine how much the effect of activity-dependent refinement should be dampened in each cell based on the decrease in Ten3 or Lphn2 in that cell compared to the amount it would express under wild-type conditions using the following formula:

$$f(x) = 1 - a \cdot \frac{x^{1/b}}{x^{1/b} + 1}$$

Where x is the absolute decrease in expression compared to wild-type conditions for that cell. For a complete list of model parameters and their description see table S1. The Koulakov model stochastically adds or removes connections to attempt to minimize a global energy value $E = E_{chem} + E_{act} + E_{comp}$ that contains three components: chemoaffinity energy (E_{chem}), activity energy (E_{act}), and competition energy (E_{comp}) where the probability of adding or removing a connection proportional to the change in energy. E_{chem} is calculated according to the following equation:

$$E_{chem} = a_{chem} \cdot \sum_{(A,D)\epsilon S_C} k_{tl} \cdot t(D) \cdot l(A) + k_{lt} \cdot l(D) \cdot t(A) - k_{tt} \cdot t(D) \cdot t(A)$$

With functions t and l describing the levels of Ten3 and Lphn2 in a given axon A or dendrite D and S_C denoting the set of all connected pairs of axons and dendrites. Meanwhile E_{act} is calculated according to:

$$E_{act} = -\frac{\gamma}{2} \sum_{(A_1,D_1),(A_2,D_2)\epsilon S_C} e^{-dist(A_1,A_2)/b_{act}} \cdot e^{-dist(D_1,D_2)^2/2a_{act}^2}$$

and E_{comp} by:

$$E_{comp} = \sum_{A\epsilon S_A} -a_{comp} \cdot \sqrt[2]{n(A)} + b_{comp} \cdot n(A)^2 + \sum_{D\epsilon S_D} d_{comp} \cdot n(D)^2$$

Where n describes the number of synapses formed by a given axon or dendrite and S_A and S_D describing the sets of all axons and dendrites respectively. In all simulations we used a linear array of 50 DH neurons across the ML axis with a matching number of DRG axons and ran the simulation for 25,000 iterations (500 steps per axon), since we found the energy E for most combinations of parameters to plateau by this point. To simulate the tracer injections, each DRG axon was given an amount of tracer according to a gaussian distribution centered at a particular PD location with the center, σ (determining the PD spread of the tracer), and concentration (determining the total amount of tracer per axon) being determined by simple grid search to best match the observed tracer distributions each ABC-SMC iteration. For simulated distal injections,

679 two gaussians were chosen to mimic the duplicated medial representation of the distal limb.
680 Parameter values for the Koulakov model were fit using ABC-SMC[68] using the PyABC package
681 (version 0.12.16)[69]. Uniform priors were used for all parameter values. PyABC was run until the
682 "epsilon over walltime" value began to plateau, with a population size of 1000, a maximum
683 number of populations equal to 10, and epsilon values determined using the quantile epsilon
684 method with the parameter alpha equal to 0.1. From this, we obtained posterior distributions over
685 the simulation parameters and a point estimate for the best model (table S1). Simulations of
686 "nerve cut" experiments[45,46] were run using the parameters from our best fit model and
687 eliminating the lateral half of axons innervating the DH. Simulations of experiments disrupting
688 activity-dependent refinement[24,26] were run using the parameters from our best fit model with an
689 80% reduction in the gamma value.

690

691 **Statistical Analysis**

692 All statistical analyses were performed in R[65] (version 4.0.5) and the specific statistical tests used
693 are described in figure legends. Figures generated in R using ggplot2[70] (version 3.4.2). The two-
694 way mixed ANOVA tests were performed using the rstatix package[71] (version 0.7.1) according to
695 the formula: fluorescence ~ genotype*position + Error(ID/position) and the genotype*position
696 interaction terms are reported.

697 **Data and code availability**

698 Code is available at (https://github.com/k-sangster/somatotopic_maps). All other data are
699 available in the main paper and supplementary materials. All materials are available through
700 requests to the corresponding author.

Acknowledgments: We thank Meirong Liang and IRCM animal facility staff for technical support; Drs. Jeffrey Mogil and Samantha Butler for comments on the manuscript; Dr. Farin Bourojeni and other members of the Kania laboratory for advice, feedback, and discussions. This work was supported by project grants from the Canadian Institutes of Health Research (CIHR; PJT-162225, MOP-77556, PJT-153053, PJT-159839, PJT-183824, and PJT-197987) to AK and National Institutes of Health (NIH; R01-NS050580) to LL. AK holds the Doggone Foundation Chair of Excellence in Pain and receives support from the Fondation IRCM. KTS is a recipient of a CIHR doctoral scholarship (FRN:494078). XZ is a recipient of a Fonds de recherche du Québec -Santé doctoral scholarship.

Author contributions: K.T.S. Performed all experiments except for the in-vitro and behavioural experiments, analysed the data, and performed the computational modelling. The in-vitro experiments were performed and analysed by D.d.T. with reagents generated by E.S. Behavioural experiments using Ten3^{KO} mice were performed by A.M.M. and D.T.P. and quantified by S.M. Behavioural experiments using Ten3$^{\Delta DH}$ mice were performed by X.Z. and quantified by C.S. R.B.R contributed to investigation and conceptualization. L.L., S.P., T.B. and C.F.B. provided reagents. A.K. supervised the study and acquired funding. A.K. and K.T.S. wrote the paper.

Competing interests: Authors declare that they have no competing interests.

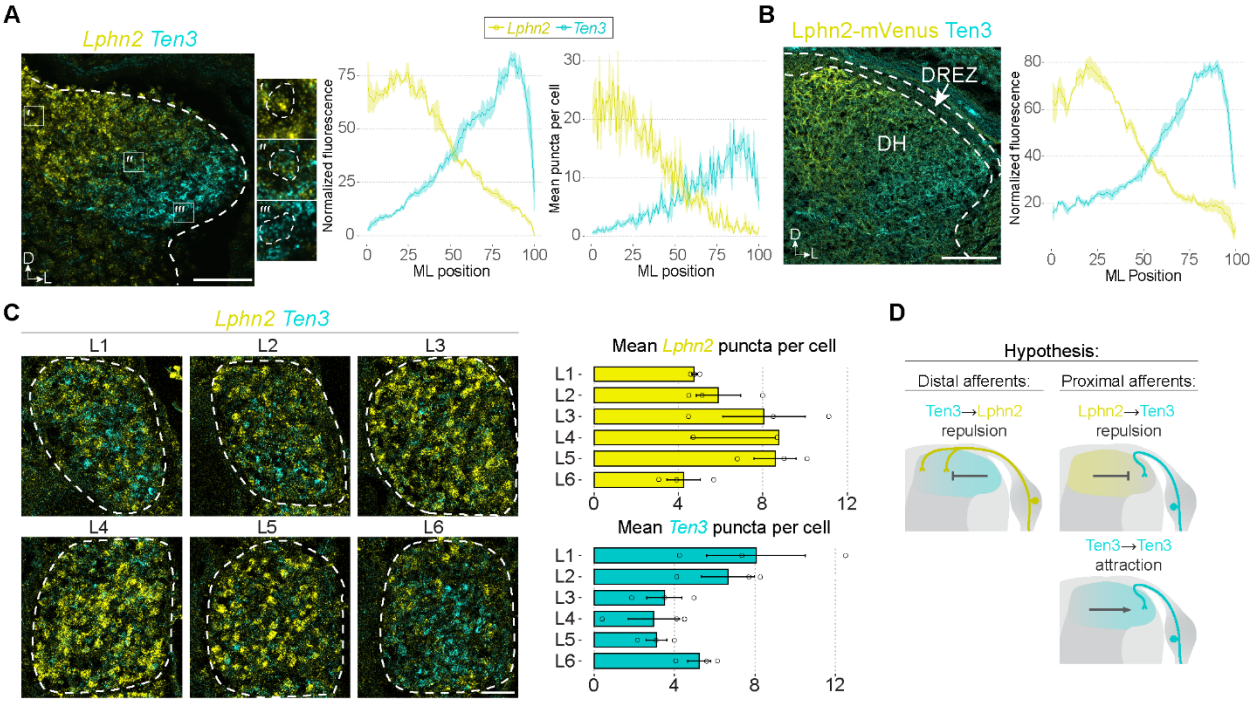

Figure 1. Complementary expression of Ten3 and Lphn2 in the DH and DRG. **A**, *Ten3* and *Lphn2* mRNA localisation in the lumbosacral DH at e14.5 (left). Quantification of RNAscope puncta and fluorescence intensity (right, n = 4 embryos). **b**, Localisation of Ten3 and Lphn2 proteins, with anti-Ten3 and anti-GFP antisera, respectively, in the lumbar DH and adjacent dorsal root entry zone (DREZ) of *Lphn2-mVenus* knock-in mice at e14.5 (left). Quantification of fluorescence intensity in the DH (right, n = 3 embryos) **C**, *Ten3* and *Lphn2* mRNA localisation in lumbar DRG at e14.5 (left) and quantification of mRNA puncta (right, n = 3 embryos). **D**, Hypothesized interactions governing DH somatotopic map formation based on the expression and previously described roles of Ten3 and Lphn2. All data shown as mean ± SEM. Scale bars in (**A**,**B**) = 100 µm, (**C**) = 50 µm. Axis labels in this and subsequent figures: M, medial; L, ventral; D, dorsal; V, ventral.

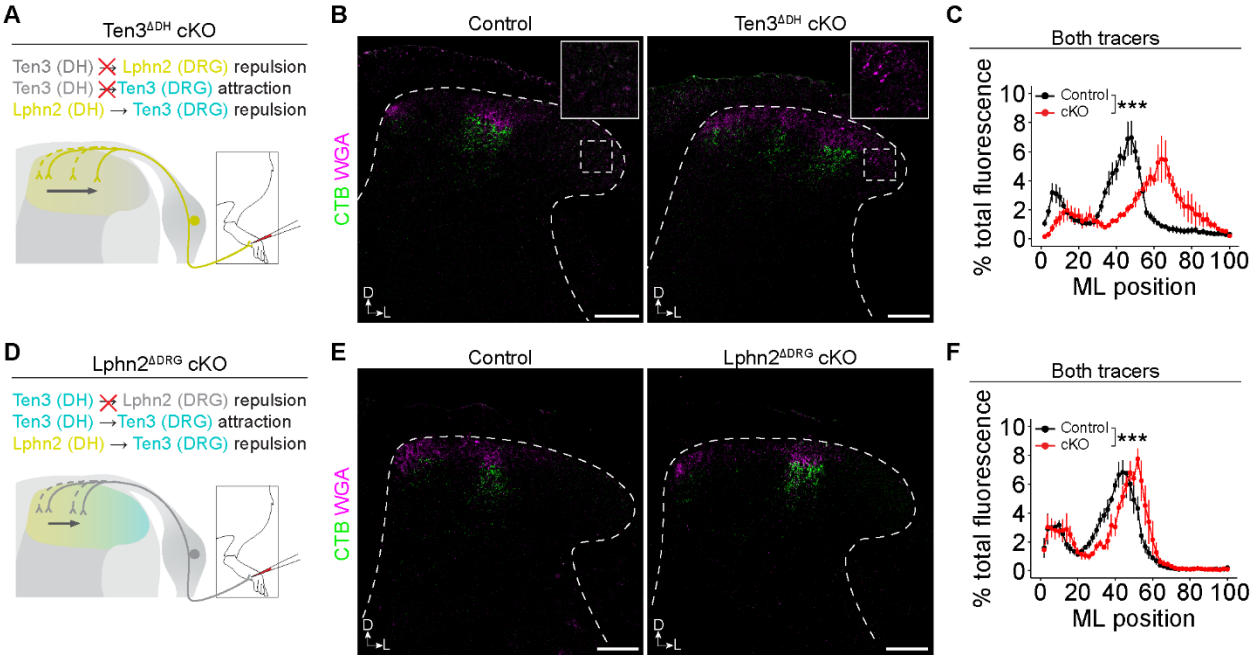

Figure 2. Aberrant somatotopy of distal sensory afferents in the DH of Ten3 and Lphn2 cKOs. A,**D**, Schematic of lost and preserved interactions in (**A**) Ten3$^{\Delta DH}$ cKOs and (**D**) Lphn2$^{\Delta DRG}$ cKOs (top) and the observed shift in the ST distribution of sensory afferents in the cKOs (bottom, filled lines) compared to controls (bottom, dotted lines). **B**,**E**, Representative images of CTB and WGA labeled afferent termini in (**B**) Ten3$^{\Delta DH}$ cKOs (insets showing WGA near lateral edge of DH in cKOs) and (**E**) Lphn2$^{\Delta DRG}$ cKOs compared to controls. Stippled lines outline the DH. **C**,**F**, Quantification of the distribution of CTB and WGA signal across the ML axis of the DH in cKOs and control littermates in (**C**) Ten3$^{\Delta DH}$ cKOs (n = 4 controls, 4 cKOs) and (**F**) Lphn2$^{\Delta DRG}$ cKOs (n = 4 controls, 3 cKOs). All data shown as mean ± SEM. Two-way mixed ANOVA was performed and genotype x bin interaction terms are reported. ***P ≤ 0.001; **P ≤ 0.01; *P ≤ 0.05. Scale bars = 100 μm.

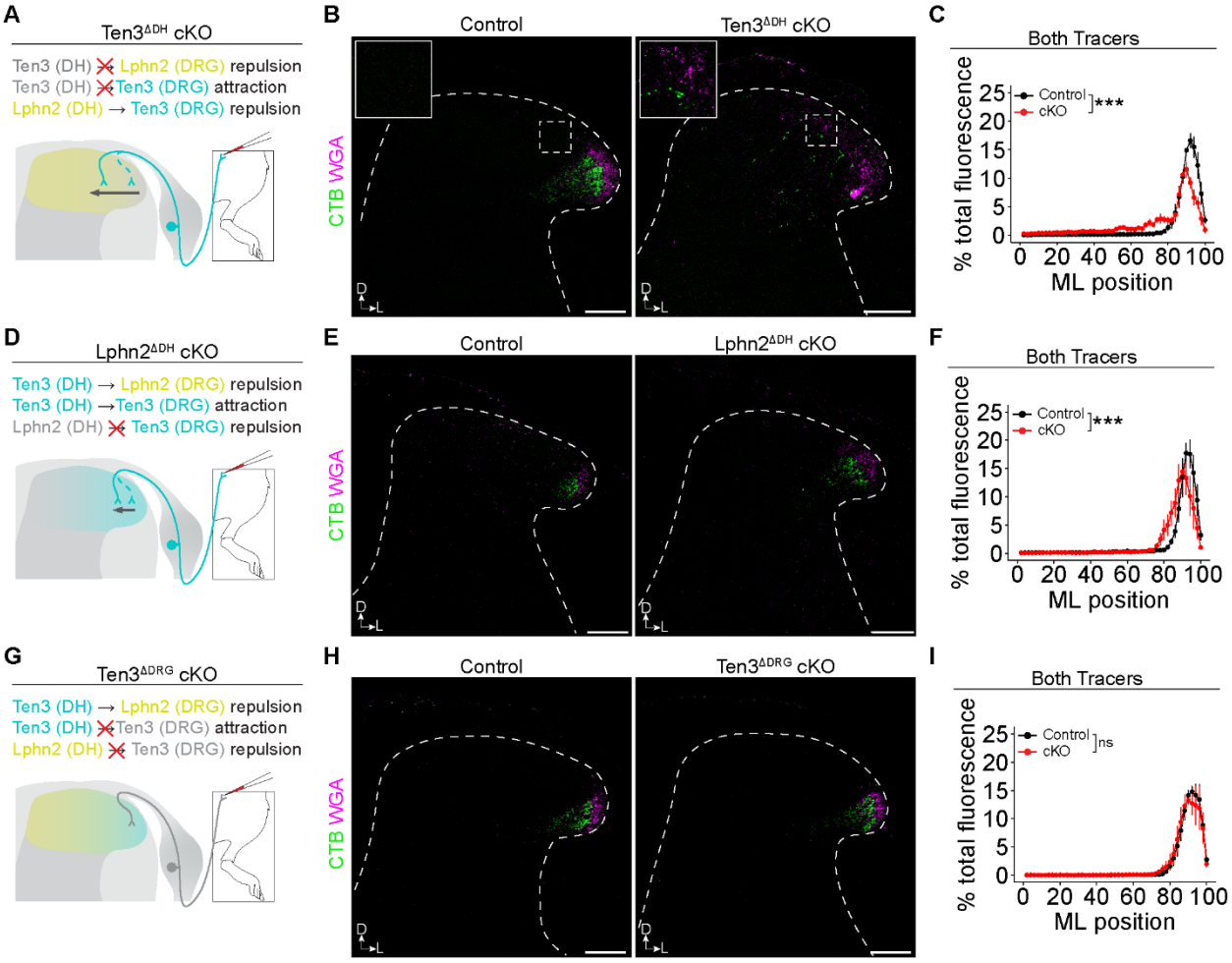

Figure 3. Altered somatotopy of proximal sensory afferents in the DH of Ten3 and Lphn2 cKOs. A, **D**, and **G**, Schematic of lost and preserved interactions in (**A**) Ten3$^{\Delta DH}$ cKOs, (**D**) Lphn2$^{\Delta DH}$ cKOs, and (**g**) Ten3$^{\Delta DRG}$ cKOs (top) and the observed shift in the ST distribution of afferent termini in the DH of cKOs (bottom, filled lines) compared to controls (bottom, dotted lines). **B**, **E**, and **H**, Representative images of CTB and WGA labeled afferents in (**B**) Ten3$^{\Delta DH}$ cKOs (insets show more medially located CTB/WGA in cKOs), (**E**) Lphn2$^{\Delta DH}$ cKOs, and (**H**) Ten3$^{\Delta DRG}$ cKOs compared to controls. Stippled lines outline the DH. **C**, **F**, and **I**, Quantification of the distribution of CTB and WGA signal across the ML axis of the DH in cKOs and control littermates in (**C**) Ten3$^{\Delta DH}$ cKOs, (**F**) Lphn2$^{\Delta DH}$ cKOs, and (**I**) Ten3$^{\Delta DRG}$ cKOs (n = 4 controls and 4 cKOs for all). All data shown as mean ± SEM. Two-way mixed ANOVA was performed

754 and genotype x bin interaction terms are reported. ***$P \leq 0.001$; **$P \leq 0.01$; *$P \leq 0.05$. Scale

755 bars = 100 μm.

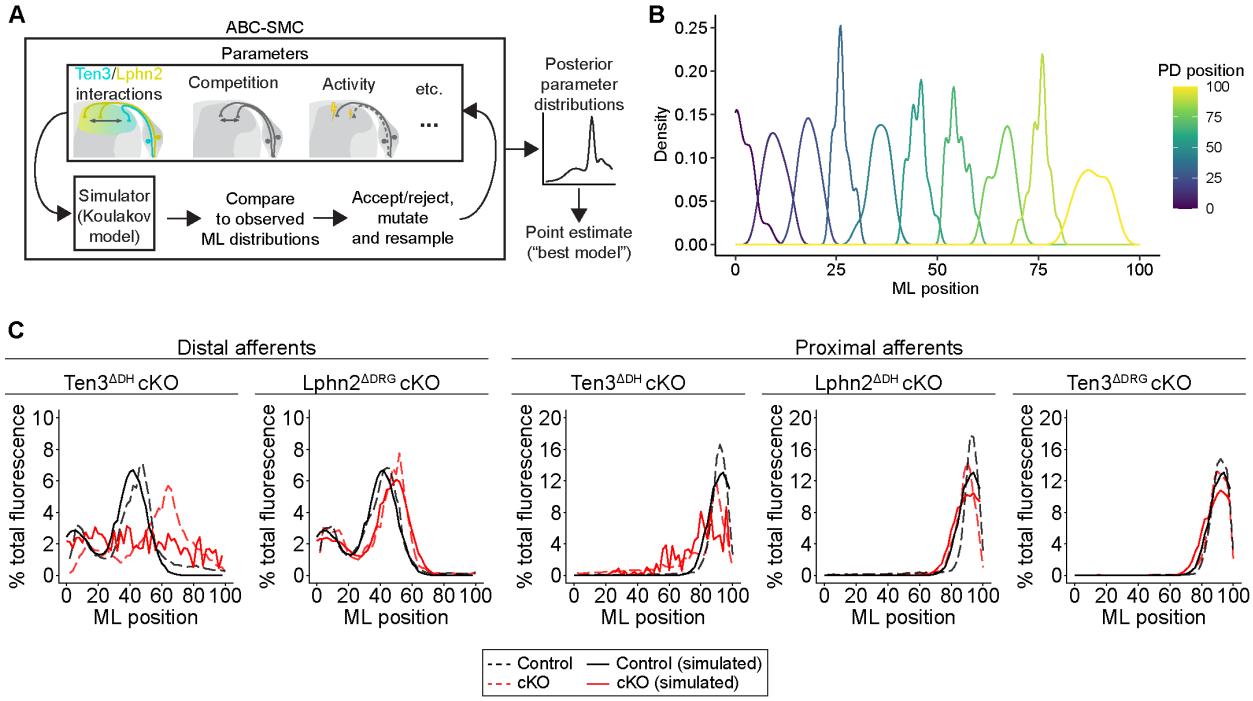

Figure 4. Computational modelling of DH somatotopic map formation. A, Simplified schematic of model parameters and of the ABC-SMC procedure. **B**, Correct distal → medial and proximal → lateral mapping from one representative simulation under wild-type conditions. Simulated ML density of terminal zones in the DH from 10 DRG axons selected across the PD axis. **C**, Observed and simulated tracer injections for controls and cKOs across all genotype/injection site combinations examined. Average distributions of each condition are shown. Simulated distribution taken from the average of 10 independent simulations.

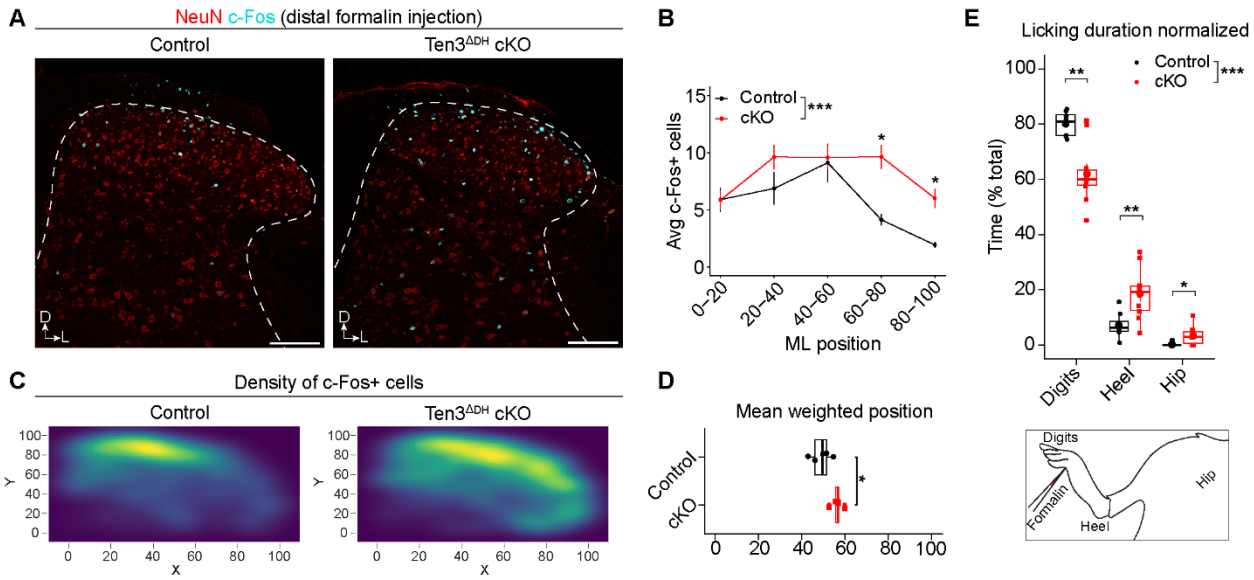

Figure 5. Altered distribution of c-Fos expression in the DH and behavioural responses induced by a noxious stimulus in Ten3$^{\Delta DH}$ cKOs. A, Representative images of c-Fos distribution in the DH induced by formalin injection to the hindpaw of Ten3$^{\Delta DH}$ cKOs and contols. **B-D**, Quantification of c-Fos-expressing cells in Ten3$^{\Delta DH}$ cKO mice and control littermates (n = 5 controls and 5 cKOs). (**B**) Distribution of c-Fos positive cells across the ML axis of the DH. Two-way mixed ANOVA test was performed, and genotype x bin interaction term is reported along with Benjamini-Yekutieli corrected post-hoc p-values for individual bin comparisons. (**C**) 2D kernel density plots showing their distribution of Fos positive cells in the DH. Hotelling T^2 p-value 0.03. (**D**) Average ML position of c-Fos-expressing cells compared with Welch's t-test. **E**, Quantification of nocifensive licking behaviour in response to formalin injection to the hindpaw near the digits, depicted as a percent of total linking time per limb region (n = 8 controls and 10 cKOs). Two-way mixed ANOVA was performed and genotype x location interaction term is reported. Post-hoc Mann-Whitney tests were performed for each limb location. All data shown as mean ± SEM. ***P ≤ 0.001; **P ≤ 0.01; *P ≤ 0.05. Scale bars = 100 µm.

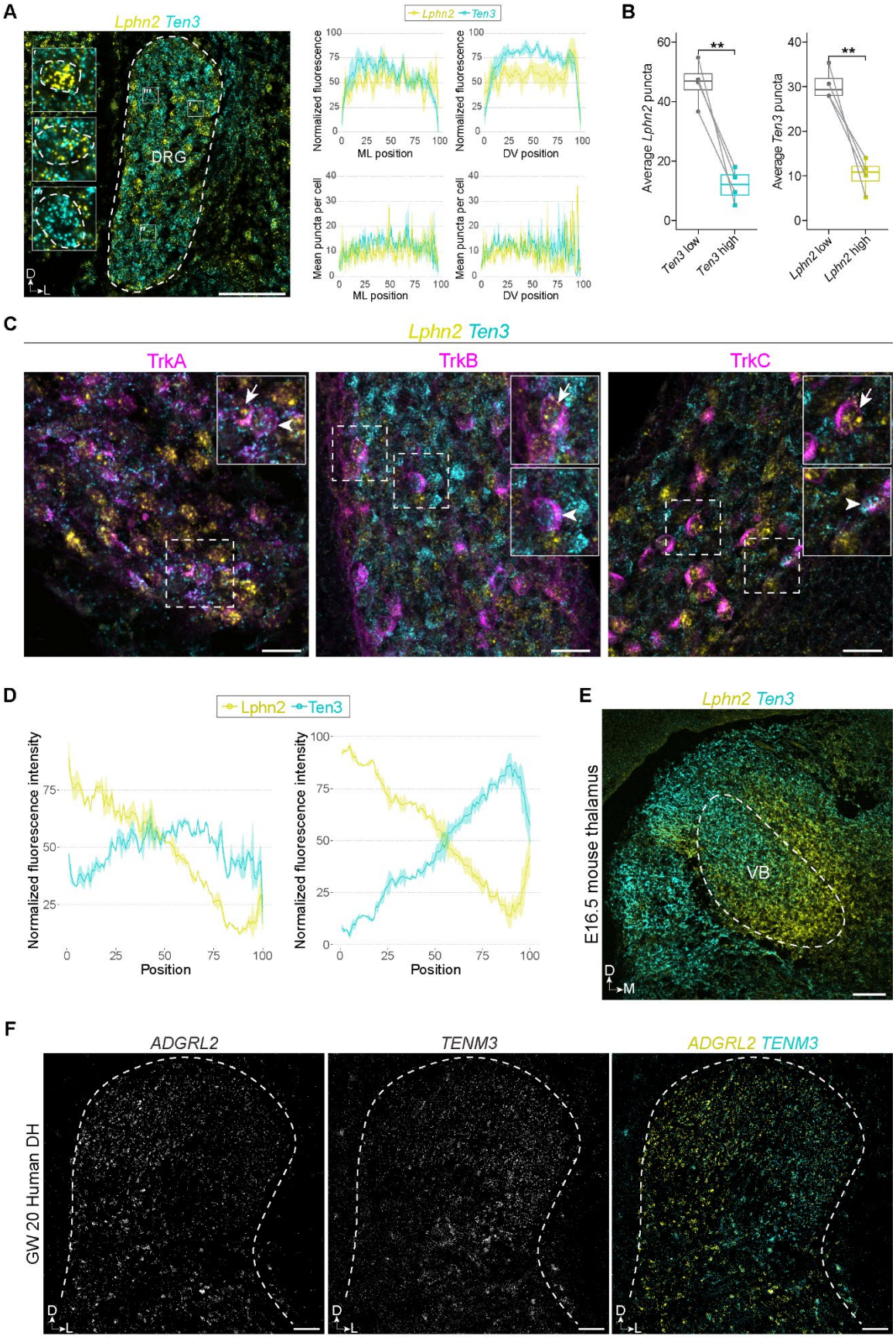
A
Lphn2 Ten3
DRG
D
L
Lphn2
Ten3
Normalized fluorescence
ML position
DV position
Mean puncta per cell
B
Average Lphn2 puncta
Average Ten3 puncta
**
Ten3 low
Ten3 high
Lphn2 low
Lphn2 high
C
Lphn2 Ten3
TrkA
TrkB
TrkC
D
Lphn2
Ten3
Normalized fluorescence intensity
Position
E
Lphn2 Ten3
E16.5 mouse thalamus
VB
D
M
F
ADGRL2
TENM3
ADGRL2 TENM3
GW 20 Human DH
D
L

Figure S1. Further characterization of Ten3 and Lphn2 expression. A, *Ten3* and *Lphn2* mRNA localisation in e14.5 DRG cross sections (left) and quantification of puncta counts and fluorescence intensity (right, n = 4 embryos) showing no spatial bias for either across the DV or ML axes. Insets show DRG neurons with high *Lphn2* (′), a mix of *Lphn2* and *Ten3* (″), and high *Ten3* mRNA levels (‴). **B**, Quantification of mRNA puncta in (A) for *Lphn2* in *Ten3*-low compared to *Ten3*-high cells and or *Ten3* in *Lphn2*-low compared to *Lphn2*-high cells. High mRNA level cells were defined as the top 90% and low mRNA cells were defined as the bottom 10% of cells expressing each respective mRNA after filtering out cells with low/no expression of both. Counts per cell were averaged such that each point corresponds to one embryo (n = 4 embryos). **C**, Dual *Ten3* and *Lphn2* mRNA and TrkA, TrkB, and TrkC DRG neuron subtype protein marker detection in e14.5 DRGs. **D**, Related to Figure 1B, quantification of fluorescence intensity of immunostaining for Ten3 and Lphn2-mVenus fusion protein (detected with an anti-GFP antibody) in the white matter adjacent to the DH of *Lphn2-mVenus* knock-in mice at e14.5 (n = 3 embryos). Shown as fluorescence intensity normalized per image (left) or as a proportion of total fluorescence intensity at each ML position (right). **E**, *Ten3* and *Lphn2* mRNA detection in the e16.5 ventrobasal (VB) thalamus aligning with the proximal to distal somatotopic organization (dorsolateral to ventromedial VB). **F**, *TENM3* and *ADGRL2* (human orthologues of *Ten3* and *Lphn2*) mRNA detection in the human gestational week (GW) 20 DH. All data shown as mean ± SEM. A paired t-test was performed in **c**. ***$P \leq 0.001$; **$P \leq 0.01$; *$P \leq 0.05$. Scale bars in **A** = 25 μm, in **B**, **E**, and **F** = 100 μm.

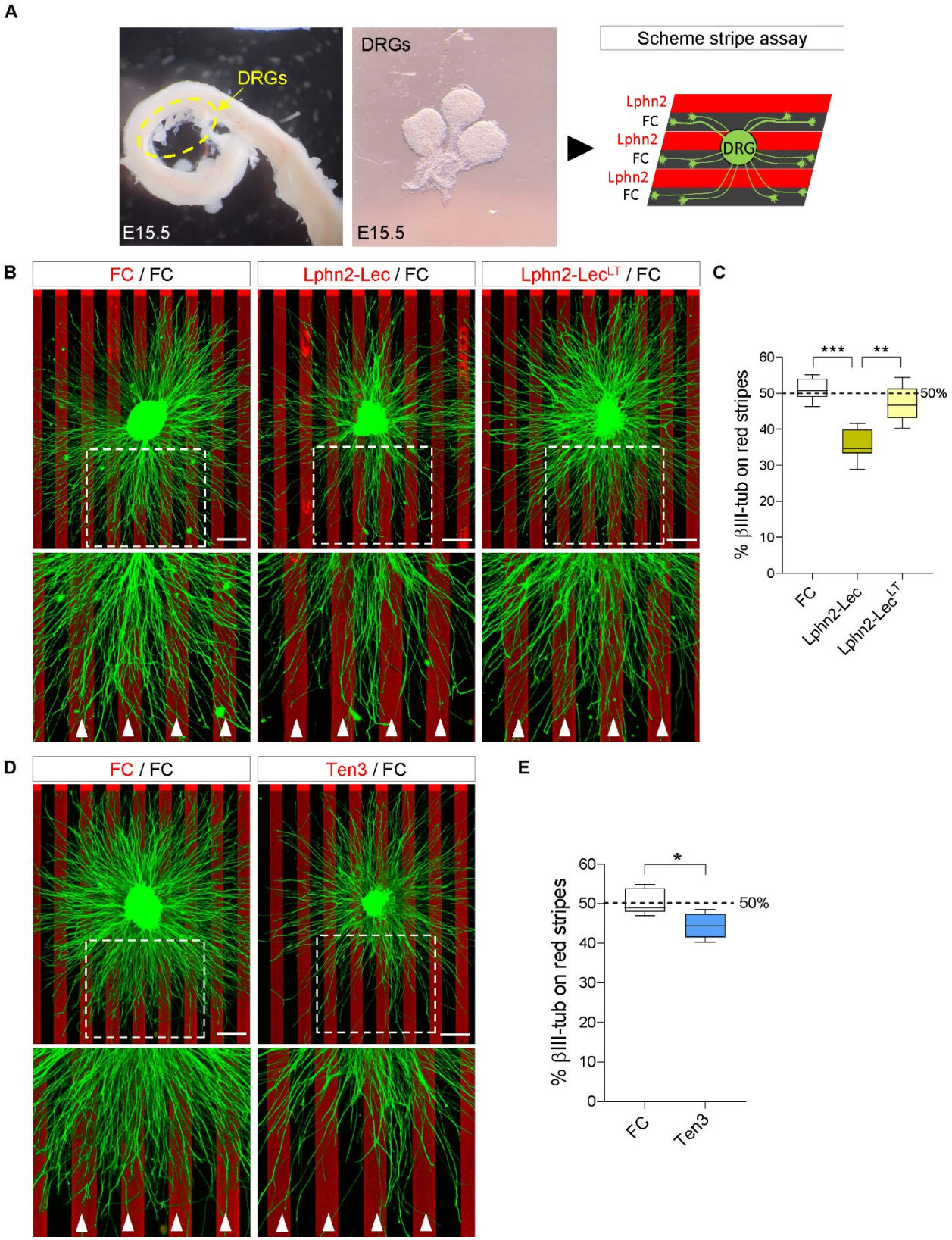
A
DRGs
E15.5
DRGs
E15.5
Scheme stripe assay
Lphn2
FC
Lphn2
FC
Lphn2
FC
DRG
B
FC / FC
Lphn2-Lec / FC
Lphn2-LecLT / FC
C
% βIII-tub on red stripes
60
50
40
30
20
10
0
***
**
50%
FC
Lphn2-Lec
Lphn2-LecLT
D
FC / FC
Ten3 / FC
E
% βIII-tub on red stripes
60
50
40
30
20
10
0
*
50%
FC
Ten3

801

802

803 **Figure S2. Ten3 and Lphn2 guide DRG axons *in vitro*. A**, Schematic of DRG explant
804 experiments. **B**, Explants of e15.5 lumbar DRGs labelled with anti-βIII-tubulin antibody,
805 cultured on stripes of: FC (black), FC (red, left), Lphn2-lectin domain (Lphn2-Lec, red, middle),
806 or Lphn2 non-Teneurin-binding mutants (Lphn2-Lec^{LT}, red, right) proteins. Red stripes are also
807 marked by white arrowheads. **C**, Quantification of βIII-tubulin protein on red stripes as a
808 percentage of the total βIII-tubulin signal. While there is no preference for red or black stripes in
809 either FC/FC or FC/ Lphn2-Lec^{LT} controls, there are significantly fewer βIII-tubulin labelled
810 axons on the red Lphn2-Lec stripes. **D**, Explants of e15.5 lumbar DRGs labelled with anti-βIII-
811 tubulin antibody grown on stripes of: FC (black), FC (red, left), or Ten3 (red, right) proteins. Red
812 stripes are also marked by white arrowheads. **E**, Quantification of βIII-tubulin on red stripes as a
813 percentage of the total βIII-tubulin signal. While there is no preference for red or black stripes in
814 FC/FC controls, there are significantly fewer βIII-tubulin labelled axons on the red Ten3 stripes,
815 indicating that despite the presumed presence of both Ten3→Lphn2 repulsion and Ten3→Ten3
816 attraction, the net effect is repulsion. ***$P \leq 0.001$; **$P \leq 0.01$; *$P \leq 0.05$. Scale bars = 200 μm.

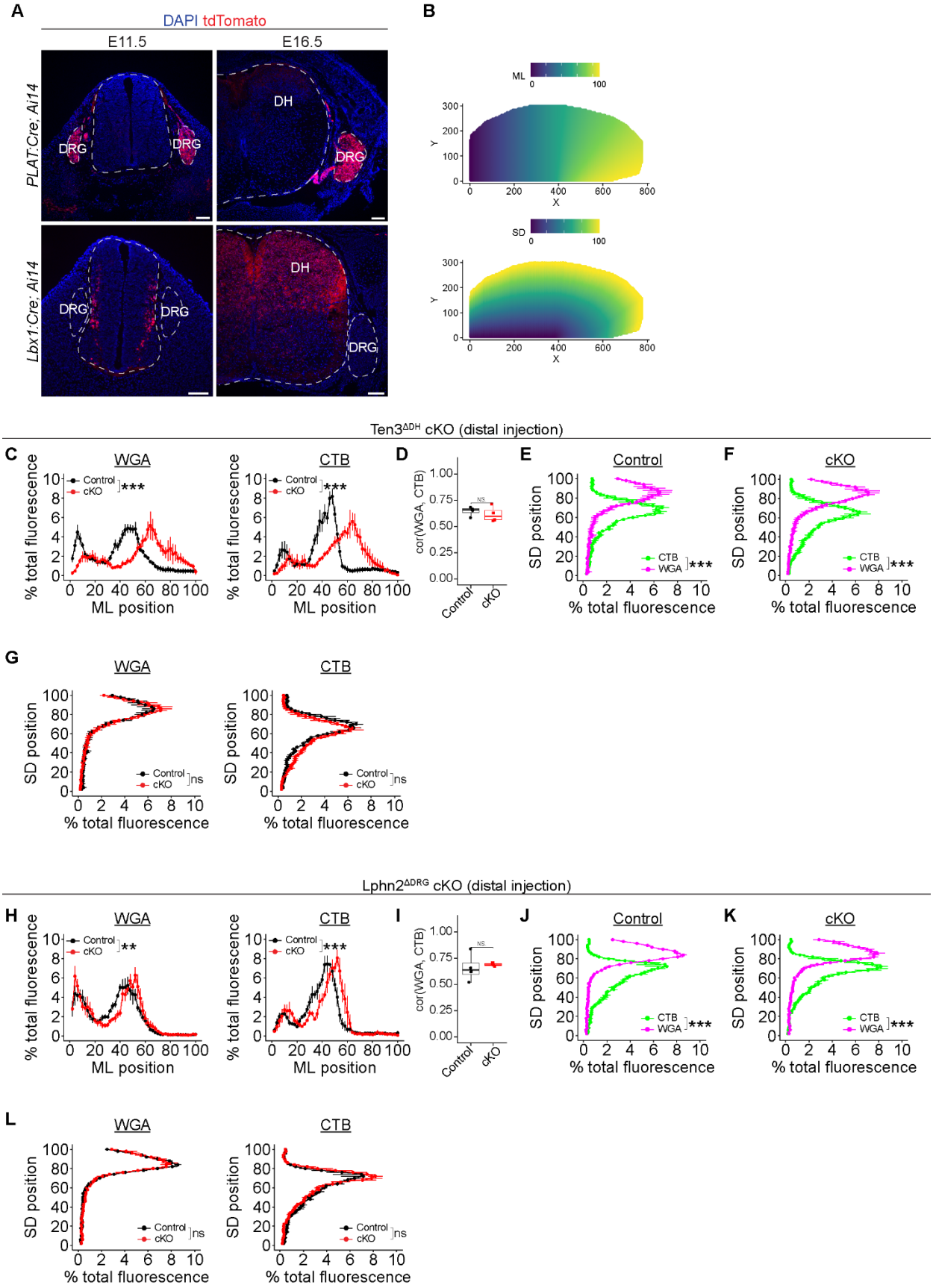
A
DAPI tdTomato
E11.5
E16.5
PLAT:Cre; Ai14
Lbx1:Cre; Ai14
DRG
DH
B
ML
SD
X
Y
Ten3ΔDH cKO (distal injection)
C
WGA
CTB
Control
cKO
% total fluorescence
ML position
D
cor(WGA, CTB)
NS
E
F
Control
cKO
SD position
CTB
WGA
G
ns
Lphn2ΔDRG cKO (distal injection)
H
I
J
K
L

818 **Figure S3. Additional characterization of distal sensory afferent termini in the DH of Ten3**
819 **and Lphn2 cKOs.** (**A**) Validation of cre driver lines used in this study showing cre-driven
820 tdTomato expression in the DH and DRG at E11.5 and E16.5 (**B**) A representative example
821 showing mapping of x and y axes to anatomically-relevant axes used in quantifications in this
822 study to account for DH curvature. (**C** and **H**) ML distribution of WGA (left) and CTB (right) in
823 (C) Ten3$^{\Delta DH}$ cKOs and (H) Lphn2$^{\Delta DRG}$ cKOs compared to littermate controls. (**D** and **I**) Average
824 Pearson correlation coefficient per animal between WGA and CTB signal across the ML axis of
825 the DH in (D) Ten3$^{\Delta DH}$ cKOs and (I) Lphn2$^{\Delta DRG}$ cKOs compared to littermate controls. (**E**, **F**, **J**
826 and **K**) SD distribution of CTB and WGA signal in controls (E and J) and cKOs (F and K)
827 showing separation along the SD axis of afferents labeled by the two tracers. (**G** and **L**) SD axis
828 distribution of WGA (left) and CTB (right) between cKOs and control littermates showing no
829 shift along this axis. All data shown as mean ± SEM. Ten3$^{\Delta DH}$, n = 4 controls and 4 cKOs;
830 Lphn2$^{\Delta DRG}$, n = 4 controls and 3 cKOs. Welch's t-test was performed in (D) and (I), in all others
831 two-way mixed ANOVA was performed and genotype x bin interaction term is reported. ***P ≤
832 0.001; **P ≤ 0.01; *P ≤ 0.05. Scale bars = 100 μm.

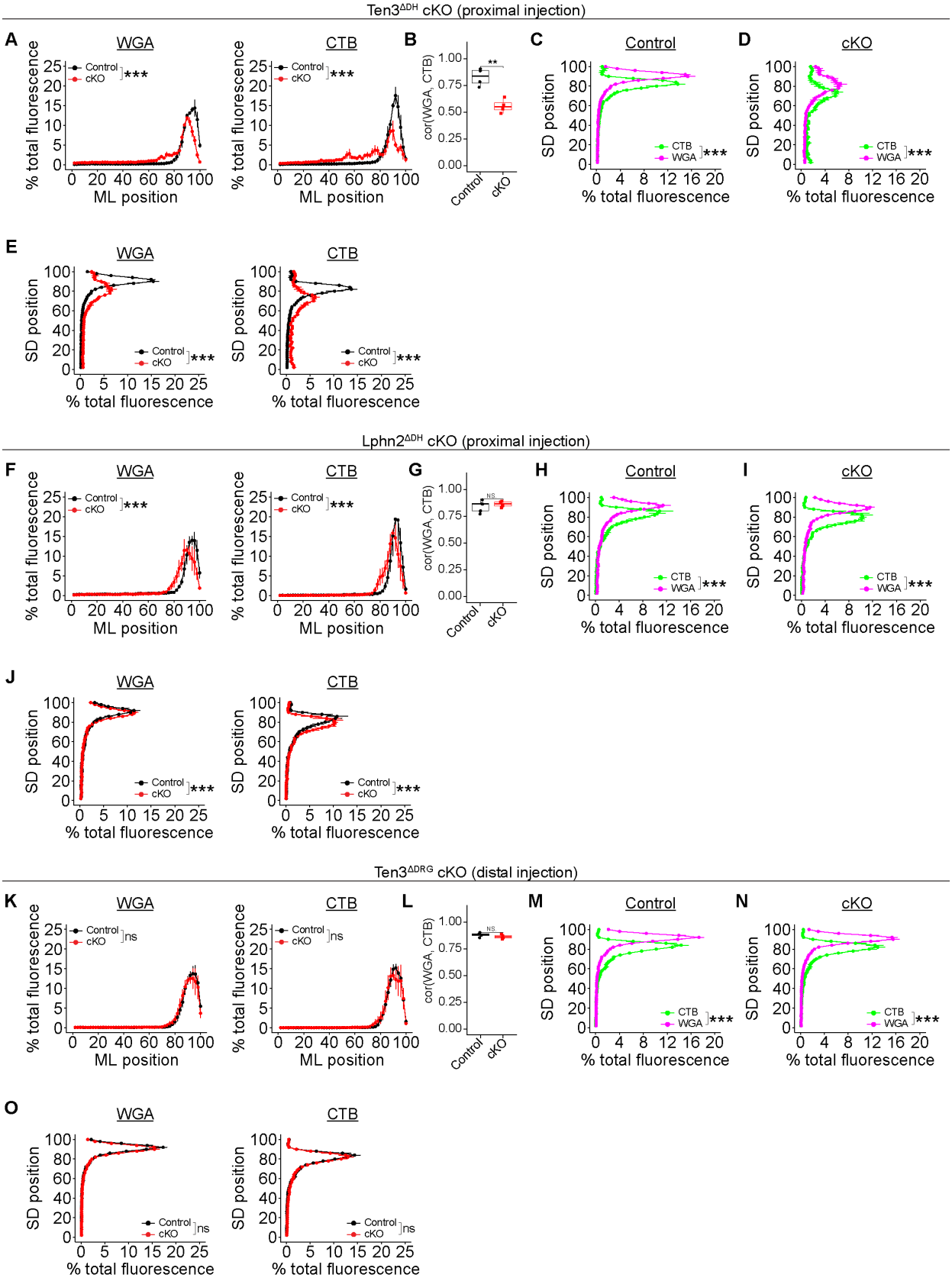
Ten3ΔDH cKO (proximal injection)
A
WGA
CTB
% total fluorescence
ML position
Control
cKO
***
B
cor(WGA, CTB)
**
C
Control
D
cKO
SD position
% total fluorescence
CTB
WGA
E
Lphn2ΔDH cKO (proximal injection)
F
G
NS
H
I
J
Ten3ΔDRG cKO (distal injection)
K
ns
L
M
N
O

833

Figure S4 Additional characterization of proximal sensory afferents in the DH of Ten3 and Lphn2 cKOs. (**A**, **F** and **K**) ML distribution of WGA (left) and CTB (right) in (A) Ten3$^{\Delta DH}$ cKOs, (F) Lphn2$^{\Delta DH}$ cKOs, and (K) Ten3$^{\Delta DRG}$ cKOs compared to littermate controls. (**B**, **G** and **L**) Average Pearson correlation coefficient per animal between WGA and CTB signal across the ML axis of the DH in (B) Ten3$^{\Delta DH}$ cKOs, (G) Lphn2$^{\Delta DH}$ cKOs, and (L) Ten3$^{\Delta DRG}$ cKOs compared to littermate controls. (**C**, **D**, **H**, **I**, **M** and **N**) SD distribution of CTB and WGA signal in controls (C, H, and M) and cKOs (D, I, and N) showing separation along the SD axis of afferent termini labeled by the two tracers. (**E**, **J** and **O**) Distribution of WGA (left) and CTB (right) long the SD axis of cKOs and control littermates. All data shown as mean ± SEM. n = 4 controls and 4 cKOs for all analyses. Welch's t-test was performed in (B), (G) and (L), in all others two-way mixed ANOVA was performed and genotype x bin interaction term is reported. ***$P \leq 0.001$; **$P \leq 0.01$; *$P \leq 0.05$.

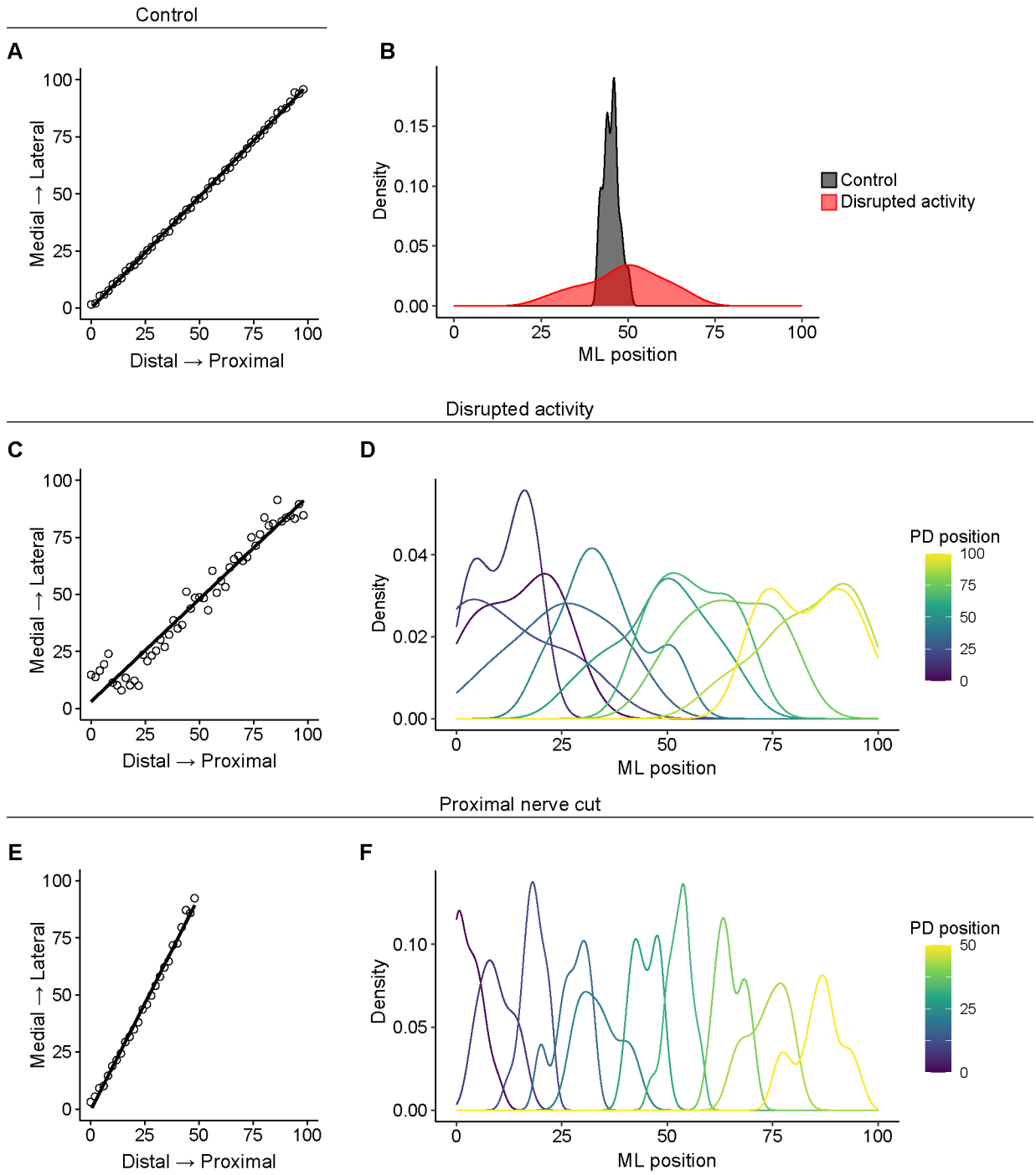
Control
A
Medial → Lateral
Distal → Proximal
B
Density
ML position
Control
Disrupted activity
Disrupted activity
C
Medial → Lateral
Distal → Proximal
D
Density
ML position
PD position
Proximal nerve cut
E
Medial → Lateral
Distal → Proximal
F
Density
ML position
PD position

846

847

848 **Figure S5. Further evaluation of computational model performance.** (**A**) PD origin of DRG
849 axons compared to the position of their ML terminal zones showing correct distal → medial and
850 proximal → lateral mapping from one representative simulation under wild-type conditions. (**B**,
851 **C**, and **D**) Simulated disruption of activity-dependent refinement from one representative
852 simulation under wild-type conditions. (B) PD origin of DRG axons compared to the position of
853 their ML terminal zones. (C) Simulated ML density of terminal zones in the DH from 10 DRG
854 axons selected across the PD axis. (D) Comparison of one terminal zone from the same axon
855 with/without disrupted activity-dependent refinement. (**E** and **F**) Simulated nerve cut experiment
856 from one representative simulation under wild-type conditions showing expansion of remaining
857 axons along the entire ML extent of the DH. (E) PD origin of DRG axons compared to the
858 position of their ML terminal zones. (F) Simulated ML density of terminal zones in the DH from
859 10 DRG axons selected across the PD axis.

860

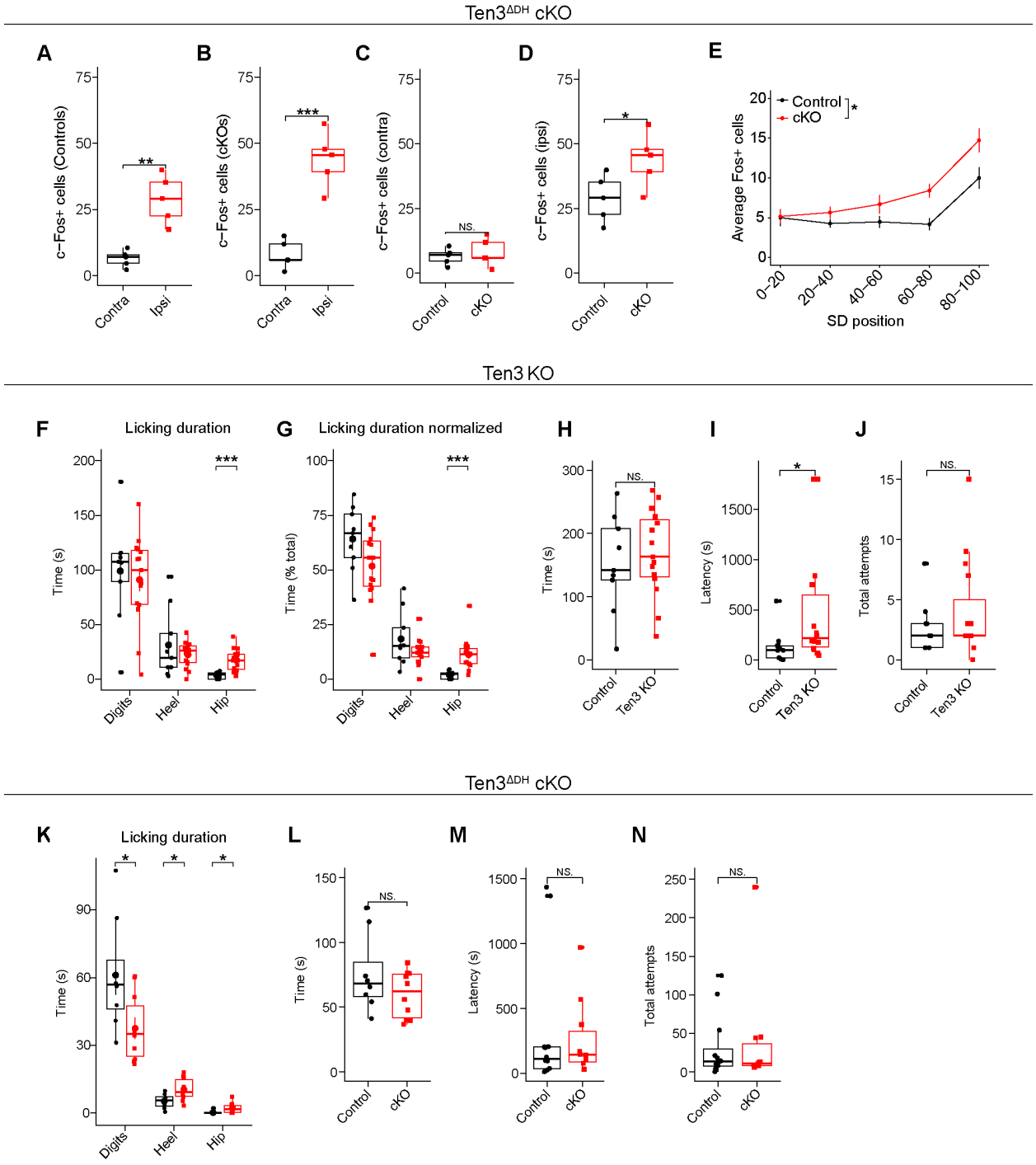
Ten3ΔDH cKO
A
c−Fos+ cells (Controls)
Contra
Ipsi
B
c−Fos+ cells (cKOs)
C
c−Fos+ cells (contra)
Control
cKO
NS.
D
c−Fos+ cells (ipsi)
E
Average Fos+ cells
SD position
0–20
20–40
40–60
60–80
80–100
Ten3 KO
F
Licking duration
Time (s)
Digits
Heel
Hip
G
Licking duration normalized
Time (% total)
H
Latency (s)
I
Total attempts
J
Ten3ΔDH cKO
K
Licking duration
L
M
N

863 **Figure S6. Additional characterization of c-Fos expression and somatosensory behavioural**
864 **responses in Ten3 mutants.** (**A** and **B**) Related to Figure 5, quantification of c-Fos-expressing
865 cells in the contralateral and ipsilateral DH relative to the side of the formalin injection in (A)
866 controls and (B) cKOs. (**C** and **D**) Quantification of c-Fos-expressing cells in cKOs compared to
867 littermate controls in the (C) contralateral and (D) ipsilateral DH relative to the site of formalin
868 injection. (**E**) SD distribution of c-Fos-expressing cells in cKOs compared to littermate controls
869 in the ipsilateral DH. (**F-H**) Quantification of nocifensive licking behavior in Ten3 global KOs
870 compared to control littermates in response to formalin injection to the hindpaw near the digits.
871 (F) The percent of total time spent licking per limb region. (G) Licking time in seconds per limb
872 region. (H) Total licking time. (**I**) Latency to remove adhesive tape from the hindpaw in KOs and
873 control littermates. (**J**) Number of attempts to remove adhesive tape from the hindpaw in KOs
874 and littermate controls. (**L-N**) Same as in panels (F), and (H-J) respectively, except performed in
875 Ten3$^{\Delta DH}$ cKOs and control littermates. All data shown as mean ± SEM. (A-E) n = 5 controls and
876 5 cKOs; (F-H) n = 9 controls and 15 cKOs, (L-N) n = 8 controls and 8 cKOs. Welch's t-test was
877 performed in (A-D) and Mann-Whitney tests were performed in (H-J) and (K-N). In (F), (G) and
878 (L) a two-way mixed ANOVA was performed, genotype x bin interaction term is reported, and
879 post-hoc Mann-Whitney tests were performed for each limb location. ***$P \leq 0.001$; **$P \leq 0.01$;
880 *$P \leq 0.05$. Scale bars = 100 μm.

Parameter category	Parameter	Value	Value in Triplett et al. 2011[8]	Description
Activity-dependent refinement	γ	1.533263	0.05	Overall strength of activity-dependent refinement
	a_{act}	3 (matched to Triplett et al.)	3	How the effect of a correlated activity scales with distance (in the target)
	b_{act}	11 (matched to Triplett et al.)	11	How the effect of a correlated activity scales with distance (in the periphery)
Competition	A_{comp}	683.569727	500	Competition term (promotes more synapses)
	B_{comp}	0.410343	1	Competition term (limits #synapses per axon)
	D_{comp}	3.152244	1	Competition term (limits #synapses per dendrite)
Chemoaffinity	α_{chem}	81.404452	20	Overall strength of "chemoaffinity" (guidance cues)
	k_{tl}	0.522447	NA	Strength of teneurin → latrophilin repulsion
	k_{lt}	0.789563	NA	Strength of latrophilin→ teneurin repulsion
	k_{tt}	0.226765	NA	Strength of teneurin → teneurin attraction
Genotype/ activity dependent refinement interaction terms	a_{t_DH}	2.991975	NA	Slope of curve describing how loss of Ten3 in the DH should affect activity dependent refinement in each cell
	b_{t_DH}	1.207797	NA	Shape of curve describing how loss of Ten3 in the DH should affect activity dependent refinement in each cell
	a_{t_DRG}	0.627226	NA	Slope of curve describing how loss of Ten3 in the DRG should affect activity dependent refinement in each cell

	b_{t_DRG}	1.532894	NA	Shape of curve describing how loss of Ten3 in the DRG should affect activity dependent refinement in each cell
	a_{l_DH}	1.505978	NA	Slope of curve describing how loss of Lphn2 in the DH should affect activity dependent refinement in each cell
	b_{l_DH}	1.250706	NA	Shape of curve describing how loss of Lphn2 in the DH should affect activity dependent refinement in each cell
	a_{l_DRG}	0.632682	NA	Slope of curve describing how loss of Lphn2 in the DRG should affect activity dependent refinement in each cell
	b_{l_DRG}	1.647495	NA	Shape of curve describing how loss of Lphn2 in the DRG should affect activity dependent refinement in each cell

Table S1. List of computational model parameters. List of parameter values derived from PyABC along with their description and corresponding value in a retinocollicular model.